miR-205-5p drives endothelial dysfunction and senescence in pulmonary fibrosis

Giuseppe Muscato[1*], Benjamin B. Roos[2*], Sharonda Harris[2], Xiaoyu Tracy Cai[2,3], Gina Civettini[2], Enrico Sciacca[1], Ahmed Raslan[4,5], Alessandra Castaldi[6], Sharon Elliot[2], Marilyn K. Glassberg[2], Carlo Vancheri[1], Daniel J. Tschumperlin[6], Giovanni Ligresti[4], Nunzia Caporarello[2,3]

Affiliations

[1]Department of Clinical and Experimental Medicine, University of Catania, Catania, Italy

[2]Department of Medicine, Stritch School of Medicine, Loyola University Chicago, Maywood, IL, United States

[3]Department of Cell and Molecular Physiology, Loyola University Chicago, Maywood, IL, US

[4]Department of Medicine, Boston University, Chobanian and Avedisian School of Medicine, Boston, MA, United States

[5] Department of Zoology, Faculty of Science, Assiut University, Assiut, Egypt

[6]Department of Medicine, University of California San Diego, La Jolla, CA, United States

[7]Department of Physiology and Biomedical Engineering, Mayo Clinic, Rochester, MN, United States

*Share first authorship

Corresponding author: Nunzia Caporarello, PhD. Department of Medicine and Department of Cell and Molecular Physiology, Loyola University Chicago, 2160 S. First Avenue, Maywood, IL, 60153; email: ncaporarello@luc.edu.

Keywords: *pulmonary fibrosis, pulmonary vasculature, lung repair, vascular aging, miRNA*

Abstract

Idiopathic Pulmonary Fibrosis (IPF) is a fatal, aging-related disease characterized by persistent lung fibroblast activation, progressive lung scarring and several vascular abnormalities. We have previously demonstrated that aging-associated vascular dysfunction drives maladaptive endothelial responses to injury and exacerbates lung fibrosis via secretion of pro-fibrotic endothelial-derived factors. However, regulatory mechanisms governing endothelial dysfunction during progressive lung fibrosis remain poorly understood. Here, using preclinical mouse models of progressive lung fibrosis as well as human IPF lungs, we demonstrate that miR-205-5p is overexpressed in lung ECs from fibrotic lungs, and coordinates gene expression programs implicated in endothelial dysfunction and progressive fibrosis. Mechanistically, miR-205-5p induces senescence in lung ECs, mirroring the senescent phenotype of IPF lung ECs. Consistently, conditioned medium derived from lung ECs overexpressing miR-205-5p promotes lung fibroblast activation. Importantly, miR-205-5p inhibition in IPF lung ECs attenuates endothelial senescence and limits paracrine fibroblast activation. Finally, inhibition of miR-205-5p in vivo preserves the pulmonary vascular network and attenuates lung fibrosis progression in aged mice challenged with bleomycin. Collectively, our findings support a novel connection between lung endothelial miR-205-5p, endothelial senescence and pro-fibrotic alteration of the endothelial secretome, and highlight miR-205-5p inhibition as a potential therapeutic intervention for pulmonary fibrosis.

Introduction

Idiopathic pulmonary fibrosis (IPF) is a progressive, aging-related disease characterized by persistent activation and sustained accumulation of scar-forming fibroblast (1, 2). IPF arises from a complex network of interactions among different cell types and profibrotic signaling pathways, making therapeutic advancement particularly challenging. Despite the ability of existing therapies to attenuate lung functional decline, they fail to halt fibrotic progression, highlighting the persistent unmet clinical need in IPF (3). While prior work has largely focused on the role of mesenchymal, epithelial and immune cell types in IPF pathogenesis and considered them as potential therapeutic targets, a growing body of evidence, including our own, supports the notion that endothelial abnormalities play a critical role in the progression of IPF (4–12). Recent work from our group has demonstrated that the pulmonary vasculature of young mice orchestrates reparative responses to lung injury by activating transcriptional programs promoting vascular repair and fibrosis resolution (7, 11). In contrast, the pulmonary vasculature of aged mice, after injury, loses this ability, and exhibits transcriptional alterations resulting into the secretion of soluble pro-fibrotic mediators, ultimately impairing fibrosis resolution. However, the mechanisms governing these maladaptive endothelial transcriptional responses to lung injury remain largely unclear. Given their capacity to modulate gene expression programs (13), microRNAs (miRNAs) are plausible candidates for influencing endothelial transcription and injury responses. Notably, miRNAs have been shown to regulate lung development and participate in the lung's response to injury, and altered levels have been implicated in the progression of chronic lung diseases, including IPF (14). Yet, their specific contribution to endothelial dysfunction in IPF remains largely unknown. To explore endothelial miRNA changes associated with lung disrepair and persistent fibrosis, we performed a miRNA screen on lung endothelial cells (ECs) freshly isolated from aged mice with progressive fibrosis and identified increased expression of miR-205-5p. Subsequent analyses confirmed increased miR-205-5p expression in lung ECs isolated from young mice with

persistent lung fibrosis induced by repetitive bleomycin injury and from human IPF lungs. In vitro studies demonstrated that miR-205-5p induces transcriptional changes in human lung ECs associated with cell cycle arrest and secretion of pro-fibrotic mediators, including components of the senescence-associated secretory phenotype (SASP), while also inducing the expression of the senescence marker β-galactosidase, mirroring the phenotype of cultured lung ECs isolated from IPF lungs. Conditioned medium from miR-205-5p overexpressing lung ECs promoted the transition of quiescent lung fibroblasts into activated fibroblasts. Integrated target prediction and network analysis identified YAP and CDKN1A signaling pathways as putative regulatory axes downstream miR-205-5p control in lung ECs. Notably, inhibition of miR-205-5p in IPF lung ECs reduced the expression of genes associated to soluble pro-fibrotic molecules belonging to the SASP, attenuated endothelial senescence and limited paracrine fibroblast activation. Importantly, inhibition of miR-205-5p in aged mice challenged with bleomycin preserved the pulmonary vascular network and attenuated lung fibrosis progression.

Taken together, our findings demonstrate that miR-205-5p plays a crucial role in perpetuating lung endothelial dysfunction and promoting a pro-fibrotic milieu driving progressive fibrosis. These data define a previously unrecognized miR-205-5p-dependent pro-fibrotic endothelial state and suggest that its targeting may represent a potential therapeutic approach in lung fibrosis.

Results

Lung endothelial miR-205-5p is upregulated in preclinical mouse models of persistent lung fibrosis and in IPF lung ECs.

Our published data documenting endothelial transcriptional changes in progressive lung fibrosis(7, 9, 11), combined with the concept that miRNAs play a pivotal role in controlling gene expression programs (15), led us to hypothesize that altered miRNAs levels may play a role in the pathogenic endothelial transcriptional programs associated with progressive lung fibrosis. To test this hypothesis, we carried out a preliminary miRNA expression screening analysis on FACS-sorted lung ECs isolated from aged mouse lungs with persistent fibrosis induced by bleomycin injury. This analysis of 84 miRNAs revealed that several miRNAs are altered in lung ECs from aged lungs, with miR-205-5p and miR-34a-5p emerging as the highest expressed miRNAs (Figure 1B). Thus, we focused on miR-205-5p and miR-34a-5p, and extended the analysis to a larger cohort of mice including young and aged mice. As shown in Figure 1C, we found that miR-205-5p and miR-34a-5p are significantly increased during progressive lung fibrosis in aged mice. Interestingly, although levels of miR-205-5p and miR-34a-5p were slightly increased in young mice injured with bleomycin compared to uninjured young mice, these increases were not significant, and levels in young mice were significantly lower compared to aged mice post-bleomycin (Figure 1C). To extend our findings to the context of human disease, we examined the expression of miR-205-5p and miR-34a-5p in lung ECs isolated from IPF lungs. Because these cells are not commercially available, we optimized our own method to isolate and culture these cells from IPF lungs with high purity, as demonstrated by immunofluorescence staining for the pan endothelial marker PECAM1 (IPF lungs obtained through Loyola University Transplant Center, Figure 2, A and B). Healthy lung ECs were isolated using the same method from donor lungs considered unsuitable for transplantation (donor lungs obtained through Gift of Hope, Illinois). Intriguingly, qPCR analysis showed significantly higher levels of miR-205-5p levels in IPF-

lung ECs compared to healthy lung ECs, whereas miR-34a-5p levels were similar in both groups (Figure 2C), identifying miR-205-5p as a candidate regulator of lung endothelial dysfunction during progressive lung fibrosis both in mice and in humans. Intriguingly, miRNAScope staining combined with immunofluorescence showed negligible miR-205-5p expression in the vasculature of healthy human lung tissue, stained using Ulex europaeus I lectin, marker for human blood vessel endothelium (16) (Figure 2D. In contrast, we found increased expression of miR-205-5p in IPF lung tissue (Figure 2D and Supplemental Figure 2), particularly in vessels closely associated to novel foci of activated fibroblasts (Figure 2D). Next, to further explore the role of endothelial miR-205-5p in progressive fibrosis, we measured its endothelial levels in an additional model of progressive fibrosis, induced by repetitive bleomycin injury in young mice. Interestingly, we found that the expression of endothelial miR-205-5p was significantly upregulated in the repetitive injury model (Supplemental Figure 1**)**, thus confirming lung endothelial miR-205-5p implication in progressive lung fibrosis. Based on these observations, we selected miR-205-5p as the candidate miRNA for our further studies.

Lung endothelial miR-205-5p controls gene programs implicated in endothelial dysfunction and induces a pro-senescent endothelial phenotype, mirroring IPF- lung ECs behavior.

To investigate the broad contribution of miR-205-5p in modulating the transcriptional landscape of lung ECs and its potential association with the aberrant endothelial phenotype in IPF, we used RNA-seq to profile gene expression in healthy lung ECs that were transfected with a miR-205-5p mimic or a negative control mimic (Figure 3A). Principal component analysis (PCA) revealed that samples clustered in two groups according to treatment (control *vs* miR-205-5p overexpression) (Figure 3B). In comparing the transcriptomes of the two groups, we identified 1208 differentially regulated genes, of which 55.7% were upregulated and 44.3% were downregulated (Figure 3C**)**. Survival and cell cycle progression genes, including *BIRC5* and *TOP2A* were significantly

downregulated by miR-205-5p overexpression (Figure 3C). In contrast, endothelial de-differentiation genes and inflammation/fibrosis genes, including *CNN1*, *TGFB2, IL1B, IGF1* and *IL1A,* were significantly upregulated in lung ECs overexpressing miR-205-5p compared to control cells (Figure 3C). Ingenuity Pathway Analysis (IPA) showed that most pathways that were downregulated by miR-205-5p overexpression (Blue bars) were associated with *Cell Cycle Checkpoint*, *Pulmonary Healing Signaling Pathways* and *Regulation of anti-oxidant/detoxification enzymes* (Figure 3D). Our analysis also led to the identification of pathways that were positively regulated by miR-205-5p overexpression (Red bars), and among them were those related to *HIF1α signaling* and *Pathogen Induced Cytokine Storm Signaling Pathway* (Figure 3D). To illustrate and compare transcriptional changes, we generated heatmaps of genes that are representative of signaling pathways implicated in endothelial cell biology and lung fibrosis that were regulated by miR-205-5p overexpression. We found that miR-205-5p downregulated several genes related to cell cycle progression, including *MKI67* (Figure 3E).). Genes associated with endothelial identity and function, such as *PECAM1*, *PLVAP*, *GPIHBP1*, and *IGF2*, as well as *NOS3* and *CCN3*, both previously shown to ameliorate vascular aging and persistent fibrosis by our group(5, 9), were also downregulated (Figure 3F.). In contrast, genes associated with endothelial de-differentiation, including *CNN2* and *TAGLN*, were upregulated in miR-205-5p overexpressing lung ECs. Moreover, genes encoding inflammatory/fibrotic secreted factors were upregulated by miR-205-5p (Figure 3G.). Among these, *TGFB2 (17)*, *PDGFA (18)*, *CSF3 (19)*, *CCL5 (20)*, *IGF1 (21)*, *IGFBP3 (22)*, and *IL1B (23),* encoding potent secreted inducers of lung fibroblast activation in IPF lungs and components of the SASP(24), were elevated. Collectively, these data implicate miR-205-5p in the regulation of cell cycle arrest, endothelial de-differentiation, and pro-inflammatory/pro-fibrotic remodeling of the endothelial secretome. Intriguingly, a similar pattern of gene expression was observed in cultured IPF lung ECs (Figure 3H), with downregulation of survival-and endothelial biology-associated genes and upregulation of several genes encoding pro-inflammatory/fibrotic secreted factors crucial for lung fibroblast

activation and IPF progression, including *IGF1*, as the most upregulated, *IGFBP3*, *TGFB2*, *PDGFA*, and *IL1B.* These findings indicate that miR-205-5p drives a transcriptional reprogramming of lung ECs that mirrors the pathological state of IPF-derived lung ECs. The combination of cell cycle arrest and increased secretion of pathogenic factors is a hallmark of cellular senescence (25), a state of stable replicative arrest implicated in IPF pathogenesis (26). Intrigued by these findings, we first confirmed reduced cell cycling by performing an immunofluorescence staining for the proliferation marker Ki67. Quantification of Ki67+ cells revealed a significant decrease in proliferating cells upon miR-205-5p overexpression (Figure 4, A and B), confirming our transcriptional data in Figure 3. Next, we evaluated senescence associated β-galactosidase (SA-β-Gal), an established senescence biomarker, and observed positive staining in lung ECs transfected with miR-205-5p (Figure 4, C and D), confirming that miR-205-5p promotes a phenotypic switch to senescence. Primary cultured IPF lung ECs also exhibited reduced Ki67 protein levels and positive SA-β-Gal (Figure 4, E-H**)**, implicating for the first time a role for senescence in human IPF lung ECs. Importantly, to support that this IPF lung EC senescent phenotype is not an artifact of culturing conditions, we analyzed publicly available sequencing dataset and confirmed that *CDKN1A*, a key marker of senescence, is upregulated in IPF lung ECs compared to healthy lung ECs (Supplemental Figure 3).

Overexpression of miR-205-5p in healthy lung ECs induces a pathogenic secretory phenotype that promotes paracrine fibroblast activation.

Given that miR-205-5p upregulates transcripts encoding secreted pro-fibrotic molecules and induces a senescent switch in lung ECs, we hypothesized that this phenotype results in the secretion of paracrine factors with pro-fibrotic activity on quiescent human lung fibroblasts. To test whether miR-205-5p overexpression in lung ECs modulates fibroblast activation via paracrine communication, we collected conditioned medium from healthy lung ECs transfected with a miR-205-5p mimic or a negative control mimic for 3 days. Human lung fibroblasts were exposed to

these conditioned media and harvested after 2 (acute exposure) or 5 (chronic exposure) days, followed by qPCR for a panel of inflammation/fibrosis-related genes (Figure 5A). Upon acute exposure, transcript levels of the inflammatory marker *IL6* were significantly upregulated, while no differences were observed in pro-fibrotic genes (Figure 5B). Intriguingly, following chronic exposure, *IL6* transcripts were downregulated to levels similar to baseline, whereas the pro-survival gene *BIRC5* and a panel of genes associated with scar-forming fibroblasts, including *CTHRC1*, *TNC*, *SPARC*, and *COL1A1* were significantly upregulated, indicating a shift from an inflammatory to a pro-fibrotic fibroblast phenotype (Figure 5C). To test whether the increase in pro-fibrotic gene expression translated into increased protein production, we performed a Collagen I deposition assay and observed significant accumulation of Collagen-I (Figure 5, D and E). Altogether, these data suggest that endothelial miR-205-5p mediates the secretion of pro-fibrotic molecules that promote the transition of quiescent fibroblasts into scar-forming fibroblast, propagating fibrosis.

miR-205-5p affects endothelial function potentially by targeting YAP and CDKN1A signaling pathways, and its inhibition in IPF lung ECs mitigates their pro-fibrotic phenotype.

Growing evidence highlights the therapeutic potential of miRNAs as a promising new class of targeted interventions. Because miRNAs can regulate several gene expression programs (27), identifying their targets in a specific biological context is crucial for understanding their function. Since our RNA-seq analysis had already identified genes downregulated by miR-205-5p overexpression (Figure 3), we first used miRTARGET, which enables enrichment analysis based on predicted miRNA–target interactions, to analyze the list of downregulated genes. This unbiased analysis confirmed miR-205-5p as the most enriched miRNA, supporting the validity of our approach (Supplemental Figure 4A). To further elucidate the mechanisms by which miR-205-5p contributes to endothelial dysfunction and fibrosis, and to restrict the analysis to genes relevant

to lung endothelial biology, we performed gene target prediction and intersected it with the significantly downregulated genes in our RNAseq. To minimize false-positive target assignments, target prediction analysis was performed with four independent target prediction platforms (TargetScan, miRTARGET, miRWalk, DIANA MicroT) and results were integrated with our RNA-seq. Thus, in downstream analyses, we only included genes that were predicted to be targets by at least two independent platforms and were significantly downregulated by miR-205-5p in lung ECs (Figure 6A). To gain mechanistic insight into the pathways regulated by miR-205-5p in the lung endothelium, we employed a network-based pathway analysis on the predicted targets (complete target list in Supplemental Table 1) . The analysis considered how predicted miR-205-5p targets interact with other genes within network pathways, providing a broad understanding of the potential impact of miR-205-5p in the lung endothelium. Intriguingly, among the regulated pathways, the YAP cascade, a key component of the Hippo signaling involved in fibrosis, was predicted to be inhibited, whereas the CDKN1A pathway, associated to cellular senescence, was predicted to be activated (Figure 6B). These findings suggest that both pathways may contribute to the pro-fibrotic phenotype induced by miR-205-5p in lung ECs. Within these pathways, we identified *YAP1* and *WWC2* as predicted targets of the YAP cascade, and *BRCA1* and *CDK19* as predicted targets of the CDKN1A cascade (Figure 6C, target alignment of miR-205-5p for predicted targets shown in Figure 6D). To extend these in silico predictions to the context of human IPF lung ECs, we performed a miR-205-5p inhibition assay and assessed the expression of the four predicted target genes. Efficient miR-205-5p inhibition was confirmed using the validated target *E2F1* (28–30) as an internal control, which showed significant upregulation following miR-205-5p inhibition (Figure 6E). Notably, *YAP1*, *WWC2* and *BRCA1* were significantly upregulated upon miR-205-5p inhibition, supporting their potential as direct targets, whereas *CDK19* expression remained unchanged (Figure 6F). Importantly, inhibition of miR-205-5p in IPF lung ECs resulted in upregulation of *BIRC5*, which we found downregulated in cultured IPF lung ECs (Figure 3H), suggesting improved endothelial survival, and in downregulation of *IGF1* (the

most upregulated pro-fibrotic gene in our analysis of IPF lung ECs), *IGFBP3,* and *IL1B* transcripts, key mediators of fibrotic remodeling in the lung and components of the SASP that were all upregulated in cultured IPF lung ECs (Figure G). While the expression of the pro-fibrotic genes *TGFB2* and *PDGFA*, as well as the endothelial identity gene *NOS3*, were not changed by the inhibition of miR-205-5p in IPF lung ECs (Supplemental Figure 4B), overall, these data suggest that inhibition of miR-205-5p in IPF lung ECs may attenuate their profibrotic phenotype. To test this hypothesis, we transfected IPF lung ECs with a negative inhibitor control or a miR-205-5p inhibitor and demonstrated increased cell proliferation, assessed as Ki67+ cells,(Figure 7, A and B) and attenuated SA-β-Gal expression (Figure 7, C and D) upon miR-205-5p inhibition in IPF cells, compared to control IPF cells transfected with a negative inhibitor control. Prompted by these data, we then tested whether miR-205-5p inhibition would mitigate the pro-fibrotic activity of the conditioned medium generated by IPF lung ECs. Intriguingly, the conditioned medium generated by IPF lung ECs transfected with a miR-205-5p inhibitor exhibited reduced paracrine pro-fibrotic activity, as demonstrated by reduced Collagen I production by human lung fibroblasts exposed to the conditioned medium generated by miR-205-5p inhibited IPF lung ECs compared to the control transfected IPF lung ECs (Figure 7, F and G). Altogether, these findings suggest that miR-205-5p impairs endothelial function potentially via the YAP and CDKN1A cascades, and that its inhibition attenuates the pro-fibrotic endothelial phenotype of IPF lung ECs, highlighting its potential as a therapeutic target.

Inhibition of miR-205-5p attenuates lung fibrosis progression in aged mice challenged with bleomycin.

Given that miR-205-5p inhibition in IPF lung ECs attenuated their pro-fibrotic phenotype, and because previous studies, including ours, showed that mitigating endothelial dysfunction reduces fibrosis progression, our next goal was to assess the therapeutic potential of miR-205-5p inhibition in bleomycin-induced chronic fibrosis in aged mice. The miR-205-5p sequence is conserved

across vertebrates, including within seed regions mediating target recognition, supporting the expectation that the effects observed in human cells would be preserved in mice. To test the effect of in vivo miR-205-5p inhibition, we delivered a specific short oligonucleutide miR-205-5p inhibitor intravenously. Successful uptake by the pulmonary vasculature was confirmed by injecting a fluorescently labeled (FAM) inhibitor via retroorbital injection followed by microscopy imaging, which detected the FAM-labeled miR-205-5p inhibitor in the pulmonary vasculature, detected via PECAM1 staining. (Supplemental Figure 5). For subsequent experiments, mice were treated with miR-205-5p inhibitor, or a negative inhibitor control, at a concentration of 10 mg/Kg (based on published evidence using the same miRNA inhibitors in preclinical mouse studies(17)) via retroorbital injection, once per week, beginning at day 14 post bleomycin delivery, after the initial inflammatory phase, based on previous findings from our group and others (31, 32), and lungs were harvested at day 30, time point associated with chronic fibrosis as previously demonstrated (7, 9) (Figure 8, A). To assess the effect of miR-205-5p inhibition on bleomycin induced lung fibrosis, we measured collagen content by hydroxyproline assay, which revealed significantly lower hydroxyproline levels in mice treated with the miR-205-5p inhibitor compared with the negative control inhibitor group (Figure 8, B). Consistently, Masson's trichrome staining revealed a reduction in collagen deposition in mice treated with miR-205-5p inhibitor (Figure 8, C). Furthermore, following bleomycin injury, regions of dense cellularity in control mice treated with the negative miRNA inhibitor exhibited reduced vessel density, consistent with our previous observations (9, 12). In contrast, miR-205-5p inhibition preserved vessel density in these regions (Figure 8, D and E), aligning with our previous findings showing that preservation of vascular integrity is associated with mitigation of bleomycin induced lung fibrosis in aged mice (12). Taken together, our findings indicate that miR-205-5p inhibition attenuates lung fibrosis progression in vivo, highlighting its potential as therapeutic avenue in lung scarring.

Discussion

Research on the contribution of vascular alterations to the pathogenesis and progression of IPF has advanced rapidly, yet significant knowledge gaps persist. Emerging evidence, including our own, have implicated dysfunctional endothelial transcriptional programs in progressive lung fibrosis (5, 7, 9–11). However, the exact mechanisms driving these transcriptional alterations remain poorly understood. miRNAs are a large family of small non-coding RNAs that have emerged as key regulators of gene expression (15). Studies have demonstrated that miRNAs participate in the regulation of multiple cellular processes and that alterations of miRNA expression are associated with the onset and progression of a plethora of human diseases (33), including IPF (34). miRNA research in IPF has primarily focused on fibroblasts, epithelial cells and macrophages. Recent research has shown that in macrophages, miR-33 is increased and regulates immunometabolic responses in IPF. In lung epithelial cells, studies have identified miR-21, let7-d and miR-26a as inducers of epithelial to mesenchymal transition and pro-fibrotic epithelial phenotypes (35–37). In fibroblasts, miR-21, miR-29 and let-7 have been identified as important miRNAs regulating fibroblast activation (38). Notably, the specific role of miRNA in regulating lung ECs gene expression during IPF remains largely unexplored.

This study is the first to profile miRNAs in fibrotic lung ECs, which are increasingly recognized as key contributors to IPF progression. Our initial miRNA screening revealed elevated levels of miR-205-5p and miR-34a-5p in ECs freshly isolated from aged mice with persistent lung fibrosis. Further analysis of lung ECs isolated from healthy and IPF lungs confirmed the overexpression of miR-205-5p, but not of miR-34a-5p, despite the miR-34 family has been implicated as promoting factor of hepatic fibrosis, thus indicating a conserved role for miR-205-5p across both murine and human fibrotic remodeling of the lung.

The role miR-205-5p has been investigated for its functions in development and cancer, where it is aberrantly expressed and may exert pro- or anti-tumorigenic roles depending on the cellular

context and target genes (28, 30, 39, 40). In lung cancer, miR-205-5p promotes tumor progression and its serum levels are significantly higher in patients compared to controls, and correlate with patient's clinical stage (40). In addition, miR-205-5p have several important effects in vascular endothelial cell function, including inhibition of angiogenesis and tube formation (41, 42). Comparatively little attention has been focused on the role of miR-205-5p in lung injury, repair and fibrosis. One recent study showed reduced miR-205-5p levels in lungs of mice with silica-induced pulmonary fibrosis and suggested that miR-205-5p could play a protective role against lung fibrosis (43). In contrast, miR-205 was found upregulated in lung tissue of IPF patients compared with controls (44), suggesting that this miRNA is implicated in progressive lung fibrosis, but that further work is needed to elucidate its overall contribution to the disease. In this work, we demonstrate that miR-205-5p induces transcriptional alterations in lung ECs, including downregulation of genes associated with cell cycle progression and endothelial identity/function, while simultaneously upregulating genes encoding secreted mediator of fibrosis and component of the SASP, a transcriptional profile that mirrors the phenotype of cultured IPF lung ECs. Further analyses confirmed that miR-205-5p induces cell cycle arrest and promotes a pro-senescent endothelial phenotype, recapitulating the behavior of lung ECs isolated from IPF lungs. Cellular senescence markers have been detected in IPF lung tissue, with established senescence biomarkers such as SA-β-galactosidase observed in both fibroblasts and epithelial cells (26). However, the contribution of endothelial senescence has remained largely unexplored. Our findings provide the first evidence of senescence in the lung endothelium of human fibrotic lungs and identify miR-205-5p as a key inducer of this pathogenic phenotype.

Cell-cell interactions are essential for coordinated responses during homeostasis and injury responses. We and others have demonstrated that lung endothelial dysfunction results in a pro-fibrotic change of the endothelial secretome (5, 7, 9–11), and senescent cells are known to secrete a broad repertoire of SASP factors that influence neighboring cells via paracrine signaling, many

of which are also pro-fibrotic mediators (26). Consistent with these observations, we found that conditioned medium from miR-205-5p overexpressing lung ECs promotes the transition of quiescent fibroblasts into scar-forming fibroblasts, indicating a novel connection between lung endothelial miR-205-5p and pro-fibrotic alterations of the endothelial secretome. Intriguingly, these effects were temporally regulated, as the 2 days acute exposure induced upregulation of the inflammatory marker IL6, whereas the 5 days chronic exposure upregulated the expression of markers of scar-forming fibroblasts. This sequential induction of inflammatory and fibrotic fibroblasts states is in agreement with recent findings demonstrating that during both mouse and human lung fibrosis, alveolar fibroblasts undergo a sequential differentiation into inflammatory and then fibrotic fibroblasts (45). These results, together with the spatial distribution of miR-205-5p in vessels adjacent to nascent fibroblast foci in IPF lung tissue, suggest that endothelial-fibroblast crosstalk induced by endothelial miR-205-5p contributes to the progression of pathogenic fibroblasts in vivo. Notably, a recent study showed that *MIR205HG*, a long noncoding RNA and host gene for miR-205, is highly expressed in aberrant basal cells, and contributes to IPF pathogenesis via upregulation of IL33 (46). Interestingly, the Authors show that miR-205 had no pro-fibrotic effects in alveolar organoids, consistent with reports that *MIR205HG* functions independently of its hosted miR-205 in other contexts (47).

Our target prediction analysis of genes downregulated following miR-205-5p overexpression in lung ECs integrated with pathways analysis highlighted the YAP and CDKN1A signaling cascades as potential contributors to the miR-205-5p-induced pro-fibrotic endothelial phenotype. Both pathways have been implicated in fibrotic remodeling of the lungs, although their specific contribution within the lung endothelium remains poorly defined. The significant overexpression of predicted target genes *YAP1*, *WWC2* (associated to the YAP pathway) and *BRCA1* (associated to the CDKN1A pathway) following inhibition of miR-205-5p in IPF lung ECs supported our findings. Although we did not observe upregulation of *CDK19,* we cannot exclude that miR-205-

5p regulates its expression at protein level in IPF lung ECs. Further mechanistic studies are warranted to confirm direct targets and determine their causative role in the pro-fibrotic endothelial phenotype induced by miR-205-5p. Given our previous findings demonstrating that activation of the YAP pathway drives fibrotic endothelial remodeling (11), defining whether and how miR-205-5p connects with this pathway will be an important avenue of future investigations. Nevertheless, our data demonstrate that inhibition of miR-205-5p in IPF lung ECs induces the expression of *BIRC5*, potentially improving endothelial survival, while concurrently suppressing key SASP and pro-fibrotic mediators *IGF1, IGFBP3* and *IL1B*, highly upregulated in IPF lung ECs and implicated in fibrotic lung remodeling. Although other pro-fibrotic genes, including *TGFB2* and *PDGFA* remained unchanged, these results collectively support the concept that miR-205-5p inhibition could mitigate endothelial dysfunction and pro-fibrotic signaling in lung fibrosis progression.

Over recent years, interest in miRNAs as therapeutic targets has grown, driven by promising results from preclinical studies in several diseases, including IPF. Notably, Chioccioli and colleagues developed a miRNA mimic to miRNA-29b that demonstrated anti-fibrotic activities both in vitro and in vivo, highlighting the potential for novel miRNA-based therapeutic approaches (48). Our in vitro data showed that inhibition of miR-205-5p in IPF lung ECs promotes cell proliferation and reduces the number of SA-β-gal positive cells, demonstrating that this strategy is effective in attenuating features of IPF endothelial dysfunction and senescence. Notably, these findings align with literature showing that other miRNAs (i.e. miR-195) can reduce the SA-β-gal expression of old mesenchymal stem cells(49). Further experiments showed that inhibition of miR-205-5p in IPF lung ECs mitigated their pro-fibrotic paracrine effects on human fibroblasts, indicating that this approach could effectively halt lung fibroblast activation and fibrosis progression. This hypothesis was validated by in vivo findings showing that miR-205-5p inhibition protects the vascular network and mitigates fibrosis progression in bleomycin induced chronic fibrosis in aged mice, highlighting the potential for future development of endothelial-targeted miRNA-based therapeutic strategies.

Although no systemic miRNA-based therapy has yet achieved regulatory approval, largely due to immune-mediated adverse events and off targets effects (50), the growing development of nanotherapeutics capable of precisely target specific lung cell types, including ECs, as recently demonstrated by our group and others (31, 51), opens new avenues for endothelial-specific miR-205-5p inhibition as a therapeutic strategy for fibrotic lung disease potentially minimizing immune-mediated adverse events and off-target extrapulmonary effects.

This study has two main limitations. First, we did not perform a small RNA-seq as initial screen, which could have revealed additional relevant miRNAs. However, our targeted approach focusing on miRNAs involved in fibrosis, inflammation, and endothelial biology, successfully identified a miRNA with a key role in lung fibrosis. Second, we did not comprehensively study the secretome induced by miR-205-5p and its relationship with the miR-205-5p targetome in lung ECs. Hence, future work will focus on directly validating the lung endothelial miR-205-5p targetome and assessing the sufficiency of candidate target genes in inducing the altered endothelial secretome downstream of miR-205-5p and identifying secreted factors and their potential interaction with cells in the alveolar niche beyond fibroblasts. Additional future directions of this work include identifying cues driving endothelial miR-205-5p upregulation and pro-fibrotic phenotype alterations. Given that miR-205 is upregulated by shear stress in models of flow induced atherosclerosis (52), and fibrotic lungs exhibit altered mechanical environment, mechanical changes likely play a role in driving its endothelial expression.

In conclusion, our in vitro and in vivo findings identify endothelial miR-205-5p as a pivotal mediator of endothelial dysfunction and driver of lung fibrosis progression. Therefore, targeting endothelial miR-205-5p, or its downstream effector pathways, represents a promising therapeutic opportunity to mitigate fibrotic remodeling in the lung.

Methods

Sex as a biological variable

Our study examined male and female mice, and similar findings are reported for both sexes. Due to limited number of patient samples used in this study, statistical adjustment for sex or gender analysis was not performed. In this study, we used lung tissue from 4 healthy donors (three males and one female) and seven IPF patients (five males and 2 females).

Patient samples

Lung tissue from IPF patients was obtained from explanted lungs obtained at the time of transplantation. All patients provided written informed consent, and the study was approved by the Loyola University Chicago Institutional Review Board (#216973). Diagnoses of IPF patients were established by clinical, radiological and pathological criteria and confirmed by multidisciplinary consensus conference. Healthy control lungs were obtained from deceased donors whose lungs were deemed unsuitable for transplant and were provided by Gift of Hope, Illinois (IRB#218010) with consent from family for tissue to be used for research purposes. No compensation was provided to subjects or family for either IPF patient samples or healthy control lungs.

Cell culture

Lung ECs from patients diagnosed with IPF, as well as non-fibrotic healthy controls were generated in-house using the following protocol. Whole lungs were mechanically and chemically digested. At least 5 grams of whole lung tissue was minced with a razor blade and transferred to 50mL conical tube with 3.75mL/gram of digestion buffer with 1.5mg/mL collagenase type IV (Worthington Biochemical Corporation), 1mg/mL collagenase type I (Worthington Biochemical Corporation), and 100U/mL of DNase I (Roche). Tissue was incubated at 37°C with rotation for

1hr. Digested tissue was filtered through sterile gauze, then 100μm cell strainer, and finally a 30μm cell strainer to obtain a single cell suspension. Whole cell suspension was pelleted, and red blood cells were lysed using 1mL red blood cell lysis buffer per gram of starting lung tissue. Red blood cell lysis buffer was neutralized with 3 volumes of PBS and cells were strained through a 30μm cell strainer. Subsequently, the whole cell suspension was pelleted and finally resuspended in Promocell Endothelial Cell Growth Medium MV2 (Promocell, Heidelberg, Germany) complete media with 1% Pen/Strep. Whole cell suspension was seeded in collagen-coated flasks (PureCol type I bovine collagen solution, Advanced BioMatrix, Carlsbad, CA, USA). When cells were confluent, CD31-dynabeads were used to purify lung ECs (Thermo Fisher Scientific, Waltham, MA, USA), that were cultured with Promocell Endothelial Cell Growth Medium MV2 (Promocell, Heidelberg, Germany). Human lung fibroblasts were purchased from Angioproteomie (Boston, MA) and cultured in DMEM/F12 with 10% FBS and 1% Pen/Strep.

Mouse studies

All animal studies were performed under protocols approved by the Mayo Clinic Institutional Animal Care and Use Committee and Loyola University Chicago's Institutional Animal Care and Use Committee and conforming to the Animal Research: Reporting of In Vivo Experiments (ARRIVE) guidelines. Col1α1-GFP transgenic mice (FVB strain) were kindly provided by Dr. Derek Radisky (Mayo Clinic, Jacksonville, FL). C57BL/6J mice were purchased from Jackson laboratory (Bar Harbor, ME, USA) or obtained via the National Institute on Aging (Baltimore, MD). Mice had access to food and water ad libitum and were on a 12/12 light/dark cycle, ambient temperature 77-78 °F and humidity 46-49%.

Mouse model of bleomycin-induced lung fibrosis

Young (two-month-old) and aged (eighteen-month-old) mice, Col1a1 GFP transgenic mice (FVB strain), both female and male, were anesthetized with a solution of ketamine (100 mg/kg) and

xylazine (10 mg/kg), injected intraperitoneally. Bleomycin 1.2 U/kg (APP Pharmaceutical, LCC Schamburg, IL, USA) or PBS were intratracheally delivered as described in our previous work (53).

For the repetitive injury model, pulmonary fibrosis was induced in young (two-month-old) C57BL/6J mice, both male and female, by six intratracheal instillation of bleomycin (0.8 U/Kg) given biweekly while mice were under isoflurane anesthesia. Mice were euthanized 3 months after the last bleomycin instillation. Mice receiving a single dose of bleomycin or PBS were used as controls. To assess the effect of miR-205-5p inhibition in mitigation of chronic fibrosis progression, we challenged eighteen-month-old C57BL/6J both male and female mice with a single dose of bleomycin, administered as described above. miRCURY Power LNA miRNA inhibitors (negative control, GeneGlobe, Cat Number: YCI0202032 - FZA, or against miR-205-5p GeneGlobe, Cat Number: YCI0201821 - FZB, Qiagen, Valencia, CA, USA - test injections with 5'FAM-labeling) were administered starting on day 14 post-bleomycin (1 intravenous retro-orbital injection, weekly, at concentration of 10 mg/Kg, based on manufacturer's indication and published evidence (54, 55)and lungs were harvested 30 days after injury, as in our previous work (31). At least five mice were instilled for each experimental condition on the basis of a power analysis to detect significant differences in fibrosis (56), numbers indicated in the figure legends.

Masson's trichrome staining

Right lobes were inflated and submerged with 10% neutral buffered formalin for 24 hours and then transferred to 70% EtOH before being paraffin embedded. Masson's Trichrome staining was performed by American Histolabs (Gaithersburg, MD, USA), or by the Research Histology Core at the University of Illinois Chicago, using 5 μm lung sections.

Fluorescence-activated cell sorting (FACS)

Mice were anesthetized with a solution of ketamine (100 mg/kg) and xylazine (10 mg/kg), injected intraperitoneally, and perfused via the left ventricle with cold PBS 30 days after bleomycin or PBS delivery. The lungs were immediately harvested and minced with a razor blade in a 100 mm petri dish in a cold DMEM medium containing 0.2 mg/ml Liberase DL and 100 U/ml DNase I (Roche, Indianapolis, IN, USA). The mixture was transferred into 15 ml tubes and incubated at 37 °C for 35 min under continuous rotation to allow enzymatic digestion. Digestion was inactivated with DMEM medium containing 10% fetal bovine serum, the cell suspension was passed through a 40 µm cell strainer (Fisher, Waltham, MA, USA) to remove debris. Cells were then centrifuged (500×g, 10 min, 4 °C) and resuspended in 3 ml red blood cell lysis buffer (Biolegend, San Diego, CA, USA) for 90 s to remove the remaining red blood cells and diluted in 9 mL PBS after incubation. Cells were then centrifuged (500×g, 10 min, 4 °C) and resuspended in 0.2 ml of FACS buffer (1% BSA, 0.5 mM EDTA pH 7.4 in PBS). For sorting, the single-cell suspension was then incubated with anti-CD45:PerCp-Cy5.5 (BioLegend Cat# 103132, RRID:AB_893340, 1:200 dilution), anti-CD31:PE (BioLegend Cat# 102407, RRID:AB_312902, 1:200 dilution), anti-EpCAM:APC (BioLegend Cat# 118213, RRID:AB_1134105, 1:200 dilution) antibodies, and DAPI (D3571, Thermo Fisher Scientific, Waltham, MA, USA, 1:1000 dilution) for 30 min on ice. After incubation, cells were washed with ice-cold FACS buffer and resuspended in 1 ml of FACS buffer. FACS sorting was conducted using a BD FACS Aria II (BD Biosciences, San Jose, CA, USA). To isolate CD45-, EpCAM-, GFP-, CD31+ population the following strategy was used: debris exclusion (FSC-A by SSC-A), doublet exclusion (SSC-W by SSC-H and FSC-W by FSC-H), dead cell exclusion (DAPI by PE), CD45 positive cell exclusion (PerCP-Cy5.5 by GFP), EpCAM and GFP positive cells exclusion (APC by GFP), and isolation of CD31 positive cells (APC by CD31) as previously described (7).

RNA isolation and miRNA screening

Total mRNA was isolated from FACS sorted CD31+ ECs isolated from mouse lungs using RNeasy micro kit (Qiagen, Valencia, CA, USA), followed by Nanodrop concentration and purity analysis. cDNA was synthesized with SuperScript VILO (Thermo Fisher Scientific, Waltham, MA, USA); miRCURY LNA miRNA Focus mouse PCR Panel was used to screen 84 miRNAs. Data represent fold changes of each miRNA relative to the aged sham and normalized to the global mean of miR-191-5p, miR-103a-3p, and miR-16-5p, stably expressed miRNAs used as reference miRNAs. Fold changes were then converted to z-scores. UniSp2, UniSp4, UniSp5, cel-miR-39-3p RNA were used as Spike-in internal controls.

Immunofluorescence

Human lung fibroblasts were seeded on coverslips and then treated for 5 days with conditioned medium generated from: 1) healthy lung ECs transfected with a negative control mimic- or a miR-205-5p mimic; 2) IPF lung ECs, transfected with a negative control inhibitor or a miR-205-5p inhibitor In experiments involving lung ECs, cells were seeded and grown on coverslips. Cells were then fixed with 10% formalin for 10 minutes at room temperature and washed three times with ice-cold PBS. Cells were then permeabilized with 0.1% Triton X-100 for 5 minutes. Following three washes with PBS, cells were incubated with blocking buffer (5% goat serum, 2% BSA) for 1 hour and then stained with Collagen I at 1:200 dilution (cat#72026, Cell Signaling Technology) for fibroblasts and Pecam1 at 1:200 dilution (Cat#3528, Cell Signaling Technology) for ECs overnight at 4°C. Next day, cells were washed three times with PBS and incubated with secondary antibodies (Cat#A11001 and Cat#A11008, Thermo Fisher Scientific, Waltham, MA, USA) at 1:1000 and containing DAPI stain (1mg/ml, dilution 1:1000) for 1 hour. Following three washes with PBS, coverslips were mounted onto slides using Aqua Poly mounting medium (Polysciences Inc, Warrington, PA, USA) and then imaged using a fluorescent microscope equipped with a camera (Olympus CKX53).

Immunohistochemistry

Formalin-fixed paraffin-embedded (FFPE) mouse lungs were cut in serial sections (7 µm). The FFPE sections were deparaffinized using a standard protocol of xylene and alcohol gradients. Sections were then blocked first with BLOXALL endogenous peroxide blocker (SP-6000-100, Vector Laboratories, Peterborough, UK) and then with 5% goat serum and 2% BSA (Sigma-Aldrich, St. Louis, MA, USA). Staining was performed using the VECTASTAIN Elite ABC HRP kit (PK-6200, Vector Laboratories, Peterborough, UK), anti-CD31 rat antibody (550274, clone MEC 13.3, BD Biosciences, 1:200 dilution) and the detection with impact DAB (Vector Laboratories, Peterborough, UK) and counterstained with Hematoxylin. Slides were then dehydrated using a standard protocol and mounted on a coverslip using DPX mounting media (Sigma-Aldrich, St. Louis, MA, USA)(20). Quantification of histochemical staining was performed using the Colour Deconvolution 2 Image J plugin on FIJI (National Institute of Health, Bethesda, MD, USA) (57). Images of stained tissue sections were acquired using identical microscope settings and color separation was performed using Colour Deconvolution 2 plugin using DAB specific stain vector. Background signal was subtracted by measuring unstained areas and thresholds were set to minimize noise. The intensity of staining was measured as integrated density Data were collected from 4-8 fields of view per sample and averaged to obtain a representative value.

miRNA scope

Paraffin lung tissue blocks were sectioned at 5-µm thickness. Sections were placed on silanized (3-aminopropyltriethoxysilane) glass slides and incubated in 10% neutral buffered formalin overnight. Slides were then washed twice in 100% ethanol, treated with 3% H_2O_2 in ethanol for 10 min at room temperature, and incubated at 110 C for 15 min in Co-Detection Target Retrieval Reagent (catalog no. 323165, Advanced Cell Diagnostics [ACD], Newark, CA). Following cooling to room temperature, slides were rinsed twice in 100% ethanol, dried for 5 min at 60 C, and marked with an ImmEdge Hydrophobic Barrier pen (catalog no. H-4000, Vector Laboratories).

Slides were treated with RNAscope Protease Plus (catalog no. 322381, ACD) for 30 min at 40 C and rinsed twice in distilled water. Subsequently, slides were processed for in situ hybridization with the miRNAscope HD (Red) Assay kit (catalog no. 324510, ACD) for human miR-205-5p (catalog no.728541). After detection of miRNAscope probes using FAST Red chromogen, slides were blocked in co-detection blocker (catalog no. 323180, ACD) and incubated overnight with Ulex lectin (CF640R/Far Red) to stain human vasculature and primary antibody against ACTA2 (VIVID520/FITC; dilution 1:100) in Co-Detection Antibody Diluent (catalog no. 323180, ACD). The following day, the slides were rinsed and mounted in Vectashield VIBRANCE Plus DAPI (catalog no. H-1800, Vector Laboratories). Digitizing was performed at the Center for Advanced Microscopy at Northwestern University. Image acquisition was performed using the TissueFAXS System (TissueGnostic). Tissue sections were outlined, and integrated density was calculated using FIJI (National Institute of Health, Bethesda, MD, USA). as previously described (46).

Transfection of negative control- and miR-205-5p mimics

Healthy lung ECs were plated at 40k cells per well of a 12-well plate in 1mL of complete media Promocell Endothelial Cell Growth Medium MV2 1%Pen/Strep (Promocell, Heidelberg, Germany). Next day, cells were transfected with mirVana negative control mimic or miR-205-5p mimic, using Lipofectamine® RNAiMAX Reagent (Thermo Fisher Scientific, Waltham, MA, USA) following manufacturers procedure to create a mimic-lipid complex in Opti-MEM Medium (all reagents were from Thermo Fisher Scientific, Waltham, MA, USA). The complex was added dropwise to each well with a final molarity of 20nM. Cells were incubated for 6 hours then the media was changed with fresh complete media. At 72 h after transfection, cells were harvested for downstream analyses.

Bulk RNA sequencing and pathway analysis

Healthy lung ECs were transfected with control- and miR-205-5p mimics. Three days after transfection, total RNA was isolated using the RNeasy Micro Kit (Qiagen, Valencia, CA, USA), following the manufacturer's instructions. RNA samples with RIN values >6 were approved for library preparation and sequencing. RNA libraries were prepared using 200 ng of total RNA. The library was validated with a 2100 Bioanalyzer (Agilent Technologies) to determine the size distribution and concentration, and sequencing was performed with a NextSeq 2000 (Illumina) at the Boston University Microarray and Sequencing Resource core facility.

FASTQ files were aligned to human genome build hg38 using STAR (version 2.7.9a). Ensembl-Gene-level counts for non-mitochondrial genes were generated using featureCounts (Subread package, version 1.6.2) and Ensembl annotation build 112 (uniquely aligned proper pairs, same strand). Variance-stabilizing transformation (VST) was accomplished using the DESeq2 R package (version 1.23.10). Principal Component Analysis (PCA) was performed using the prcomp R function with VST-normalized expression values that were then *z*-score-normalized (set to a mean of zero and a standard deviation of one) across all samples within each gene. Differential gene expression was assessed using raw count data with the Wald test implemented in the DESeq2 R package. Correction for multiple hypothesis testing was accomplished using the Benjamini-Hochberg false discovery rate (FDR). All analyses were performed using the R environment for statistical computing (version 4.1.2). Pathway analyses were carried out using differentially expressed genes with Ingenuity Pathway Analysis (IPA) software (QIAGEN, Valencia, CA, USA). Heatmaps were created using Prism 9 (GraphPad Software) using VST values *z*-score-normalized across all samples within each gene.

RNA isolation and qPCR analysis

Total mRNA was isolated using RNeasy Micro Kit (Qiagen, Valencia, CA, USA), followed by Nanodrop concentration and purity analysis. cDNA was synthesized with SuperScript VILO (Thermo Fisher Scientific, Waltham, MA, USA); RT-PCR was performed using FastStart Essential DNA Green Master (Roche Diagnostics, Mannheim, Germany) and analyzed using a QuantStudio3 (Thermo Fisher Scientific, Waltham, MA, USA). qPCR primers used in this study (Integrated DNA Technologies, Coralville, IA, USA) are listed in Table 1. miRNAs assays used in this study (Thermo Fisher Scientific, Waltham, MA, USA) are U6 (Assay ID 001973), miR-205-5p (Assay ID 477967_mir) and miR-34a-5p (Assay ID 478048_mir).

miR-205-5p inhibition in IPF lung ECs

IPF lung ECs were plated at 50k cells per well of a 12-well plate in 1mL of complete media Promocell Endothelial Cell Growth Medium MV2 1%Pen/Strep (Promocell, Heidelberg, Germany). Next day, cells were transfected with mirVana negative control inhibitor or mir205-5p inhibitor using Lipofectamine® RNAiMAX Reagent following manufacturers procedure to create a mimic-lipid complex in Opti-MEM Medium (all reagents were from Thermo Fisher Scientific, Waltham, MA, USA). The complex was added dropwise to each well with a final molarity of 100nM. Cells were incubated for 6 hours then the media was changed with fresh complete media. At 48 h after transfection, cells were harvested for RNA isolation and qPCR analysis.

Ki67 Staining

Human lung ECs (isolated from healthy or IPF lungs; or healthy lung ECs transfected with a control mimic or with a miR-205-5p mimic; or IPF lung ECs transfected with a negative inhibitor control or a miR-205-5p inhibitor) were washed, fixed and permeabilized in 0.1% Triton X-100 for 5 minutes at room temperature. Cells were then blocked with 4% goat serum for 1 hour and primary Ki67 (Santa Cruz Biotechnology Cat. # sc-23900, 1:100 dilution, Dallas, TX, RRID: AB 627859) antibody solution was added for an overnight incubation at 4°C. Cells were then washed

with PBS and secondary antibody solution of Alexa Fluor 488 goat anti-mouse (Thermo Fisher Scientific Cat. No. A-11001, 1:500 dilution, Waltham, MA, RRID:AB_2534069) and counterstained with DAPI (Biolegend, Cat. No. 422801, 1:1,000 dilution, San Diego, CA) was added for 2 h at room temperature. All antibodies were commercially available and were validated by the respective manufacturers. Fluorescence images of Ki67- and DAPI-stained cells were analyzed using the JaCoP (Just Another Colocalization Plugin) plugin in ImageJ version 1.54g (National Institute of Health, Bethesda, MD, USA). Prior to analysis, images were background-subtracted, and thresholds were set to minimize noise. Colocalization between Ki67 and nuclear DAPI signals was then quantified, and Pearson's correlation coefficient was calculated to assess the degree of nuclear localization of Ki67. At least 10 fields per condition were analyzed to ensure reproducibility.

Senescence-Associated β-Galactosidase Staining

Human lung ECs (healthy or IPF-derived; healthy transfected with a control mimic or with a miR-205-5p mimic; IPF transfected with a negative inhibitor control or a miR-205-5p inhibitor) were plated in 8 well chambered slides and SA-β-Galactosidase staining was performed per the manufacturer's protocol (Senescence β-Galactosidase Staining kit Cat# 9860, Cell Signaling Technology). Briefly, cells were washed with PBS and 1X fixative solution was added for 15 minutes at room temperature. Fixative was washed away with PBS and cells were stained with β-Galactosidase staining solution (pH 6.0). Chambers were sealed with a plate cover to prevent evaporation and crystal formation, and incubated in the absence of CO_2 in a dry 37°C incubator for 12hrs. β-Galactosidase staining solution was removed and cells were rinsed with PBS and stained with DAPI (1:1000) for 1 hour at RT. The chambers were removed, and slides were cover slipped and imaged using an optical microscope and a 10X objective. For quantification, phase contrast images of SA-β-Galactosidase staining were first taken, followed by DAPI fluorescent

images. Blue-stained cells and total number of DAPI positive cells were counted and data plotted as percentage of SA-β-galactosidase positive cells/total number of cells in each field of view.

Single-cell RNA sequencing and data analysis

Publicly available human scRNA-seq dataset from Tsukui et al (GSE132771) (58) were analyzed using Bio Turing Browser X. CD31+ ECs from healthy human lungs and IPF lungs were included in the analysis and displayed as violin plot.

Isolation and testing of endothelial-derived conditioned medium

Healthy lung ECs were transfected using mirVana negative control mimic or miR-205-5p mimic, IPF lung ECs were transfected using mirVana negative control inhibitor or miR-205-5p inhibitor (as described above). Media was replaced 6 h after transfection to remove the transfection reagents and cells were cultured for 72 h. Conditioned media from control- and miR-205-5p overexpressing cells was then collected and centrifuged at 1,100 rpm for 5 min to remove cellular debris before being applied to human lung fibroblasts. After 2 days or 5 days, RNA isolation and qPCR were performed as described in *RNA isolation and qPCR analysis*. After 5 days, Collagen-I staining was performed as described in Immunofluorescence.

Target prediction analysis

The enrichment of genes among predicted targets of the indicated miRNAs was determined by uploading the list of genes downregulated in the miR-205-5p mimic lung ECs experiment into MiRTARGET. Target prediction was carried out using four independent tools (miRTARGET (59), miRWalk (60), TargetScanHuman (61), DIANA-MicroT (62)) and target prediction lists were integrated with the list of genes downregulated in miR-205-5p mimic in the lung ECs experiment. The resulting gene lists were further integrated and only downregulated genes predicted to be target by at least two bioinformatic tools were included in downstream analysis.

Statistical Analysis

The individual data points shown in all plots represent data from individual mice or biological replicates from cell culture experiments. Sample size for each experimental group is reported in figure legends. Variables were summarized by mean and standard deviation with statistical comparisons between groups performed using Student's t-test or one-way analysis of variance (followed by Tukey's or Dunnet's post hoc test). All analyses and plots were generated with GraphPad 10 (La Jolla, CA, USA) with statistical significance defined as $p < 0.05$ (GraphPad Prism, RRID:SCR_002798).

Study approval

The study was approved by the Loyola University Chicago Institutional Review Board (#216973). Lung tissue was obtained from IPF explanted lungs, from individuals who provided a written informed consent. Healthy control lungs were obtained from deceased donors whose lungs were deemed unsuitable for transplant and were provided by Gift of Hope, Illinois (IRB#218010) with consent from family for tissue to be used for research purposes.

Data availability

The RNA-seq data Discussed in this publication have been deposited in NCBI's Gene Expression Omnibus and are accessible through GEO Series accession number GSE316481 (https://www.ncbi.nlm.nih.gov/geo/query/acc.cgi?acc=GSE316481). The Supporting Data Values file contains all quantifications performed and showed in plots. All supporting data values are available in Supplemental Material online with this article.

Author contributions

G.M. and B.B.R. contributed equally to this work and are listed in alphabetical order. G.M., B.B.R. and N.C. conceived and designed research; G.M., B.B.R., E.S., A.R., S.H., X.T.C. G.C. performed experiments; G.M., B.B.R., A.C. and N.C. analyzed data; G.M., B.B.R. and N.C. interpreted data; G.M., A.C. and N.C. prepared figures; G.M. and N.C. drafted the manuscript; D.J.T., G.L., and N.C. edited the manuscript; G.M., B.B.R., S.H., X.T.C., G.C., E.S., A.R., C.V., A.C., S.E., M.K.G., D.J.T., G.L., N.C. approved final version of manuscript.

Funding Support

This work is the result of NIH funding, in whole or in part, and is subject to the NIH Public Access Policy. Through acceptance of this federal funding, the NIH has been given a right to make the work publicly available in PubMed Central. A Shared Instrumentation Grant from the National Institutes of Health (1S10OD034431-01) at Loyola University Chicago supported this work. We gratefully acknowledge support for this work by the National Institutes of Health (NIH) grants R01 HL092961 (to D.J.T.), R01 HL166187 (to D.J.T.) and R01 HL158733 (to G.L.).

Acknowledgments

We would like to acknowledge support from the Boston University Microarray and Sequencing Resource Core Facility, with particular thanks to Yuriy Alekseyev. miRNA scope service was provided by the Northwestern University Mouse Histology and Phenotyping Laboratory, which is supported by National Cancer Institute grant no. P30-CA060553, awarded to the Robert H. Lurie Comprehensive Cancer Center. Histology services were provided by the Research Histology Core at the University of Illinois Chicago, part of the Research Resources Center, which was established with support from the Office of the Vice Chancellor for Research. Imaging Data was generated using EvidentVS200 in the Pathology Department Research Tissue Imaging Facility at University of Illinois at Chicago.

References

1. Lederer DJ, Martinez FJ. Idiopathic Pulmonary Fibrosis. *New England Journal of Medicine*. 2018;378(19):1811–1823.

2. Spagnolo P, et al. Pulmonary fibrosis secondary to COVID-19: a call to arms? *Lancet Respir Med*. 2020;8(8):750–752.

3. Bonella F, Spagnolo P, Ryerson C. Current and Future Treatment Landscape for Idiopathic Pulmonary Fibrosis. *Drugs*. 2023;83(17):1581–1593.

4. Adams TS, et al. Single-cell RNA-seq reveals ectopic and aberrant lung-resident cell populations in idiopathic pulmonary fibrosis. *Sci Adv*. 2020;6(28). https://doi.org/10.1126/sciadv.aba1983.

5. Betageri KR, et al. The matricellular protein CCN3 supports lung endothelial homeostasis and function. *American Journal of Physiology-Lung Cellular and Molecular Physiology*. 2023;324(2):L154–L168.

6. Bian F, et al. Lung endothelial cells regulate pulmonary fibrosis through FOXF1/R-Ras signaling. *Nat Commun*. 2023;14(1):2560.

7. Caporarello N, et al. Dysfunctional ERG signaling drives pulmonary vascular aging and persistent fibrosis. *Nat Commun*. 2022;13(1):4170.

8. Caporarello N, Ligresti G. Vascular Contribution to Lung Repair and Fibrosis. *Am J Respir Cell Mol Biol*. 2023;69(2):135–146.

9. Caporarello N, et al. Vascular dysfunction in aged mice contributes to persistent lung fibrosis. *Aging Cell*. 2020;19(8). https://doi.org/10.1111/acel.13196.

10. Knipe RS, et al. Endothelial-Specific Loss of Sphingosine-1-Phosphate Receptor 1 Increases Vascular Permeability and Exacerbates Bleomycin-induced Pulmonary Fibrosis. *Am J Respir Cell Mol Biol*. 2022;66(1):38–52.

11. Raslan AA, et al. Lung injury-induced activated endothelial cell states persist in aging-associated progressive fibrosis. *Nat Commun*. 2024;15(1):5449.

12. Gianì F, et al. Vascular protection by young circulating extracellular vesicles ameliorates aging-related pulmonary fibrosis. *American Journal of Physiology-Cell Physiology*. 2025;329(1):C159–C169.

13. Rupaimoole R, Slack FJ. MicroRNA therapeutics: towards a new era for the management of cancer and other diseases. *Nat Rev Drug Discov*. 2017;16(3):203–222.

14. Stolzenburg LR, Harris A. The role of microRNAs in chronic respiratory disease: recent insights. *Biol Chem*. 2018;399(3):219–234.

15. Shang R, et al. microRNAs in action: biogenesis, function and regulation. *Nat Rev Genet*. 2023;24(12):816–833.

16. Holthöfer H, et al. Ulex europaeus I lectin as a marker for vascular endothelium in human tissues. *Lab Invest*. 1982;47(1):60–6.

17. Sun T, et al. TGFβ2 and TGFβ3 isoforms drive fibrotic disease pathogenesis. *Sci Transl Med*. 2021;13(605). https://doi.org/10.1126/scitranslmed.abe0407.

18. Zhou Y, Ling T, Shi W. Current state of signaling pathways associated with the pathogenesis of idiopathic pulmonary fibrosis. *Respir Res*. 2024;25(1):245.

19. Kim S, et al. Colony-stimulating factor 3 as a key mediator in the progression of idiopathic pulmonary fibrosis: a novel therapeutic target. *Signal Transduct Target Ther*. 2025;10(1):322.

20. Choi ES, et al. Enhanced monocyte chemoattractant protein-3/CC chemokine ligand-7 in usual interstitial pneumonia. *Am J Respir Crit Care Med*. 2004;170(5):508–15.

21. Hernandez DM, et al. IPF pathogenesis is dependent upon TGFβ induction of IGF-1. *FASEB J*. 2020;34(4):5363–5388.

22. Pilewski JM, et al. Insulin-like growth factor binding proteins 3 and 5 are overexpressed in idiopathic pulmonary fibrosis and contribute to extracellular matrix deposition. *Am J Pathol*. 2005;166(2):399–407.

23. Leung LY, et al. A new microrheometric approach reveals individual and cooperative roles for TGF-beta1 and IL-1beta in fibroblast-mediated stiffening of collagen gels. *FASEB J*. 2007;21(9):2064–73.

24. Saul D, et al. A new gene set identifies senescent cells and predicts senescence-associated pathways across tissues. *Nat Commun*. 2022;13(1):4827.

25. Kumari R, Jat P. Mechanisms of Cellular Senescence: Cell Cycle Arrest and Senescence Associated Secretory Phenotype. *Front Cell Dev Biol*. 2021;9. https://doi.org/10.3389/fcell.2021.645593.

26. Schafer MJ, et al. Cellular senescence mediates fibrotic pulmonary disease. *Nat Commun*. 2017;8(1):14532.

27. Lin J, et al. Polarization-controlled tunable directional coupling of surface plasmon polaritons. *Science*. 2013;340(6130):331–4.

28. Vosgha H, et al. miR-205 targets angiogenesis and EMT concurrently in anaplastic thyroid carcinoma. *Endocr Relat Cancer*. 2018;25(3):323–337.

29. Martínez-Santos M, et al. Role of Exosomal miR-205-5p Cargo in Angiogenesis and Cell Migration. *Int J Mol Sci*. 2024;25(2):934.

30. Chen X, et al. MiR-205-5p Functions as a Tumor Suppressor in Gastric Cancer Cells through Downregulating FAM84B. *J Oncol*. 2022;2022:1–10.

31. Betageri KR, et al. Lung-targeted Lipid Nanoparticle Delivery of a Matricellular mRNA Promotes Fibrotic Lung Repair. *Am J Respir Cell Mol Biol*. [published online ahead of print: October 14, 2025]. https://doi.org/10.1165/rcmb.2025-0247OC.

32. Meridew JA, et al. Optimized Synthetic Flavonols Support Senescence Clearance and Lung Fibrosis Resolution. *ACS Pharmacol Transl Sci*. 2025;8(9):3033–3046.

33. Oliveira AC, et al. Understanding the Modus Operandi of MicroRNA Regulatory Clusters. *Cells*. 2019;8(9):1103.

34. Zhou Z, et al. Revisiting the role of MicroRNAs in the pathogenesis of idiopathic pulmonary fibrosis. *Front Cell Dev Biol*. 2024;12:1470875.

35. Liang H, et al. Integrated analyses identify the involvement of microRNA-26a in epithelial-mesenchymal transition during idiopathic pulmonary fibrosis. *Cell Death Dis*. 2014;5(5):e1238.

36. Pandit K V, et al. Inhibition and role of let-7d in idiopathic pulmonary fibrosis. *Am J Respir Crit Care Med*. 2010;182(2):220–9.

37. Yamada M, et al. The increase of microRNA-21 during lung fibrosis and its contribution to epithelial-mesenchymal transition in pulmonary epithelial cells. *Respir Res*. 2013;14(1):95.

38. Elliot S, et al. MicroRNA let-7 Downregulates Ligand-Independent Estrogen Receptor–mediated Male-Predominant Pulmonary Fibrosis. *Am J Respir Crit Care Med*. 2019;200(10):1246–1257.

39. Ferrari E, Gandellini P. Unveiling the ups and downs of miR-205 in physiology and cancer: transcriptional and post-transcriptional mechanisms. *Cell Death Dis*. 2020;11(11):980.

40. Zhao Y, et al. MiR -205-5p promotes lung cancer progression and is valuable for the diagnosis of lung cancer. *Thorac Cancer*. 2022;13(6):832–843.

41. Liu J, et al. MiR-195-5p and miR-205-5p in extracellular vesicles isolated from diabetic foot ulcer wound fluid decrease angiogenesis by inhibiting VEGFA expression. *Aging*. 2021;13(15):19805–19821.

42. Oltra M, et al. Oxidative stress-induced angiogenesis is mediated by miR-205-5p. *J Cell Mol Med*. 2020;24(2):1428–1436.

43. Qian Q, et al. MicroRNA-205-5p targets E2F1 to promote autophagy and inhibit pulmonary fibrosis in silicosis through impairing SKP2-mediated Beclin1 ubiquitination. *J Cell Mol Med*. 2021;25(19):9214–9227.

44. McDonough JE, et al. Transcriptional regulatory model of fibrosis progression in the human lung. *JCI Insight*. 2019;4(22). https://doi.org/10.1172/jci.insight.131597.

45. Tsukui T, Wolters PJ, Sheppard D. Alveolar fibroblast lineage orchestrates lung inflammation and fibrosis. *Nature*. 2024;631(8021):627–634.

46. Takashima T, et al. Involvement of lncRNA MIR205HG in idiopathic pulmonary fibrosis and IL-33 regulation via Alu elements. *JCI Insight*. 2025;10(5). https://doi.org/10.1172/jci.insight.187172.

47. Profumo V, et al. LEADeR role of miR-205 host gene as long noncoding RNA in prostate basal cell differentiation. *Nat Commun*. 2019;10(1):307.

48. Chioccioli M, et al. A lung targeted miR-29 mimic as a therapy for pulmonary fibrosis. *EBioMedicine*. 2022;85:104304.

49. Okada M, et al. Abrogation of Age-Induced MicroRNA-195 Rejuvenates the Senescent Mesenchymal Stem Cells by Reactivating Telomerase. *Stem Cells*. 2016;34(1):148–59.

50. What will it take to get miRNA therapies to market? *Nat Biotechnol*. 2024;42(11):1623–1624.

51. Deng Z, et al. Fluorinated amphiphilic Poly(β-Amino ester) nanoparticle for highly efficient and specific delivery of nucleic acids to the Lung capillary endothelium. *Bioact Mater*. 2024;31:1–17.

52. De Rosa S, et al. Flow-Responsive Noncoding RNAs in the Vascular System: Basic Mechanisms for the Clinician. *J Clin Med*. 2022;11(2). https://doi.org/10.3390/jcm11020459.

53. Jones DL, et al. ZNF416 is a pivotal transcriptional regulator of fibroblast mechanoactivation. *Journal of Cell Biology*. 2021;220(5). https://doi.org/10.1083/jcb.202007152.

54. Chen T, et al. MicroRNA-212-5p, an anti-proliferative miRNA, attenuates hypoxia and sugen/hypoxia-induced pulmonary hypertension in rodents. *Mol Ther Nucleic Acids*. 2022;29:204–216.

55. Yuan T, et al. Combinatorial miRNA1a/15b interference drives adult cardiac regeneration [preprint]. 2024. https://doi.org/10.1101/2024.04.10.24305521.

56. Redente EF, et al. Persistent, Progressive Pulmonary Fibrosis and Epithelial Remodeling in Mice. *Am J Respir Cell Mol Biol*. 2021;64(6):669–676.

57. Ruifrok AC, Johnston DA. Quantification of histochemical staining by color deconvolution. *Anal Quant Cytol Histol*. 2001;23(4):291–9.

58. Tsukui T, et al. Collagen-producing lung cell atlas identifies multiple subsets with distinct localization and relevance to fibrosis. *Nat Commun*. 2020;11(1):1920.

59. Rokavec M, Hermeking H. miRTARGET: An integrated web tool for the identification of microRNA targets with potential therapeutic or prognostic value in cancer. *Neoplasia*. 2025;67:101202.

60. Sticht C, et al. miRWalk: An online resource for prediction of microRNA binding sites. *PLoS One*. 2018;13(10):e0206239.

61. McGeary SE, et al. The biochemical basis of microRNA targeting efficacy. *Science*. 2019;366(6472). https://doi.org/10.1126/science.aav1741.

62. Tastsoglou S, et al. DIANA-microT 2023: including predicted targets of virally encoded miRNAs. *Nucleic Acids Res*. 2023;51(W1):W148–W153.

Figure legends

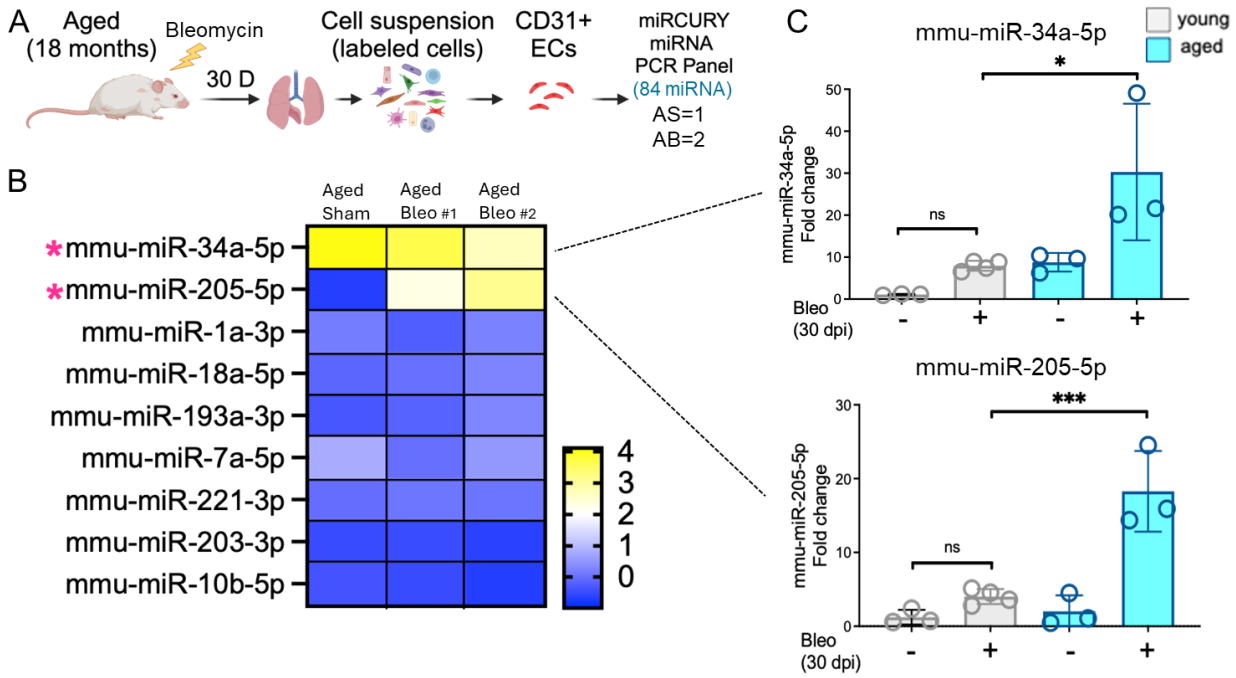

Figure 1. miRNA expression profile of lung ECs from aged mice with persistent lung fibrosis. A) Experimental workflow: aged mice intratracheally received bleomycin (1.2 U/kg); lungs were collected on day 30, dissociated into single cells, and CD31⁺ lung ECs were isolated by FACS (created with a licensed version of BioRender.com). **B)** Endothelial miRNA expression was quantified using a miRNA focus qPCR panel including 84 miRNAs. Heatmap showing the top 9 differentially expressed, with miR-205-5p and miR-34a-5p emerging as the most upregulated (Aged Sham, n=1; Aged Bleo, n=2, displayed as z-score). **C)** qPCR confirmed significant upregulation of miR-205-5p and miR-34a-5p in FACS sorted CD31+ lung ECs from aged mice 30 days after bleomycin exposure compared to young mice under the same experimental condition. snU6 was used as normalization control. Data are represented as mean ± SD, and each dot represents an individual mouse (Y sham n=3, Y Bleo n=4, A sham n=3, A Bleo n=3). p values were calculated using one-way analysis of variance (followed by Tukey's post hoc test). *p<0.05; ***p<0.001.

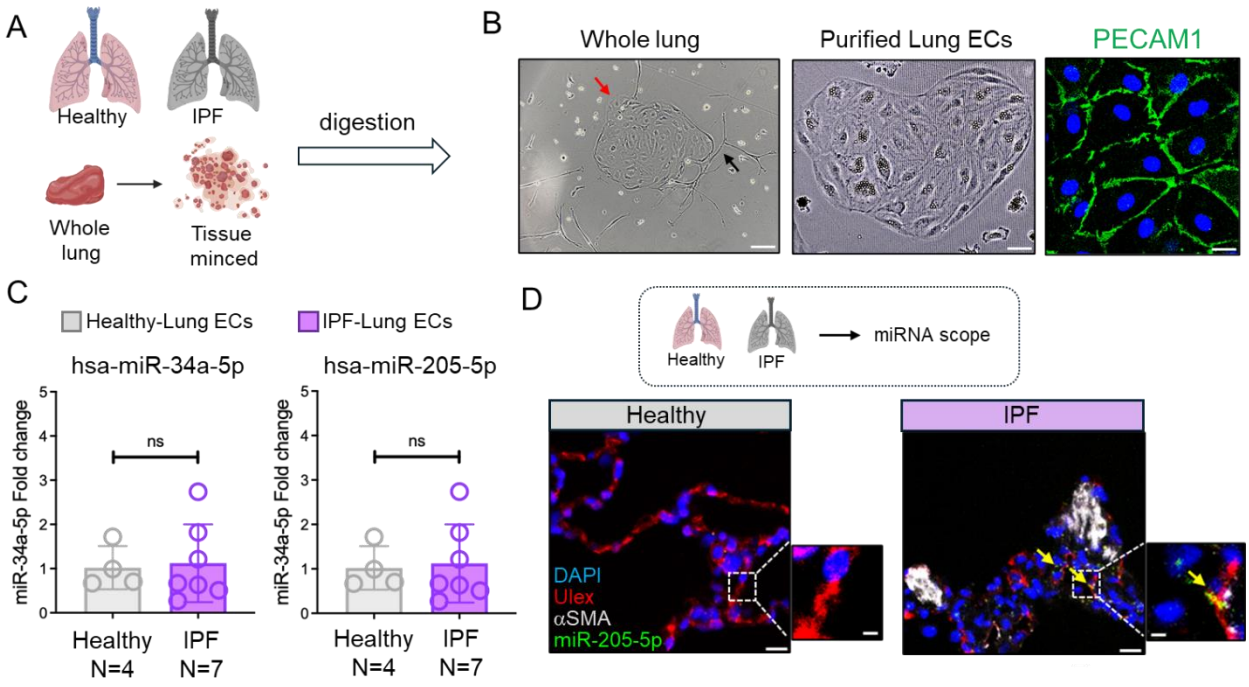

Figure 2. Lung endothelial miR-205-5p is overexpressed in IPF lung ECs and co-localizes with vessels near fibroblastic foci. **A)** Schematic depicting our novel isolation protocol employed to purify lung ECs from control and IPF lungs (created with a licensed version of BioRender.com). **B)** Purified lung ECs express the pan-endothelial marker PECAM1 (green). **C)** qPCR shows higher levels of miR-205-5p in IPF lung ECs compared to healthy lung ECs, whereas no difference is observed in miR-34a-5p levels. snU6 was used as normalization control. Data are shown as mean ± SD (healthy n=4 donors, IPF n=7 patients) and p values were calculated using Student's t-test. * P<0.05. **D)** Representative combined immunofluorescence and miRNA Scope images of one healthy lung tissue and one IPF lung tissue. Ulex europaeus I lectin was used to stain vessels, (red), αSMA antibody as marker of activated fibroblasts (white), miR-205-5p probe to detect human miR-205-5p, DAPI for nuclei (Blue). Scale bar: 50μm.

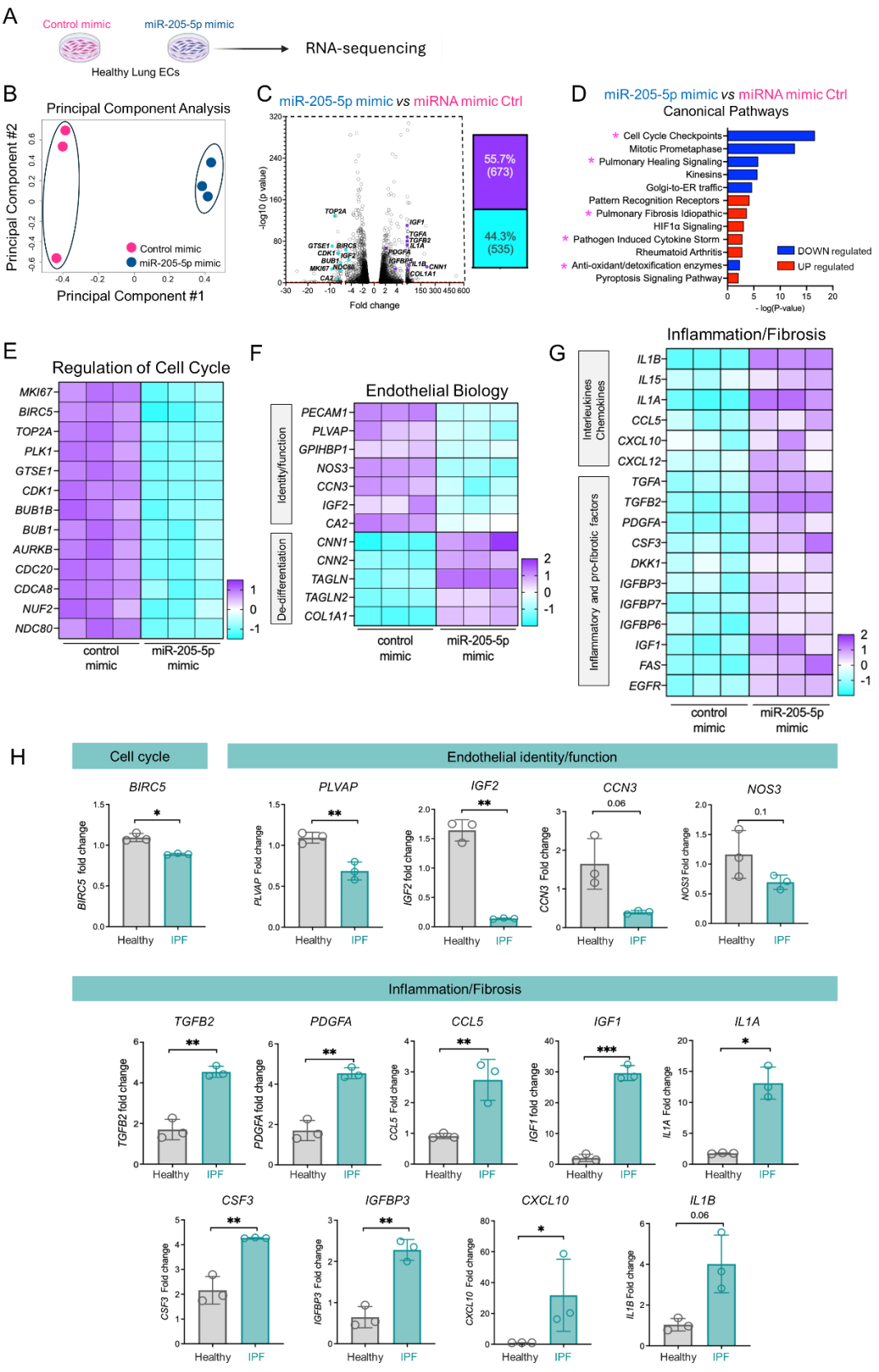
A
Control mimic
miR-205-5p mimic
RNA-sequencing
Healthy Lung ECs
B
Principal Component Analysis
Principal Component #2
Principal Component #1
Control mimic
miR-205-5p mimic
C
miR-205-5p mimic vs miRNA mimic Ctrl
-log10 (p value)
Fold change
55.7% (673)
44.3% (535)
D
miR-205-5p mimic vs miRNA mimic Ctrl
Canonical Pathways
Cell Cycle Checkpoints
Mitotic Prometaphase
Pulmonary Healing Signaling
Kinesins
Golgi-to-ER traffic
Pattern Recognition Receptors
Pulmonary Fibrosis Idiopathic
HIF1α Signaling
Pathogen Induced Cytokine Storm
Rheumatoid Arthritis
Anti-oxidant/detoxification enzymes
Pyroptosis Signaling Pathway
DOWN regulated
UP regulated
- log(P-value)
E
Regulation of Cell Cycle
MKI67
BIRC5
TOP2A
PLK1
GTSE1
CDK1
BUB1B
BUB1
AURKB
CDC20
CDCA8
NUF2
NDC80
control mimic
miR-205-5p mimic
F
Endothelial Biology
Identity/function
De-differentiation
PECAM1
PLVAP
GPIHBP1
NOS3
CCN3
IGF2
CA2
CNN1
CNN2
TAGLN
TAGLN2
COL1A1
control mimic
miR-205-5p mimic
G
Inflammation/Fibrosis
Interleukines Chemokines
Inflammatory and pro-fibrotic factors
IL1B
IL15
IL1A
CCL5
CXCL10
CXCL12
TGFA
TGFB2
PDGFA
CSF3
DKK1
IGFBP3
IGFBP7
IGFBP6
IGF1
FAS
EGFR
control mimic
miR-205-5p mimic
H
Cell cycle
Endothelial identity/function
BIRC5
PLVAP
IGF2
CCN3
NOS3
Healthy
IPF
Inflammation/Fibrosis
TGFB2
PDGFA
CCL5
IGF1
IL1A
CSF3
IGFBP3
CXCL10
IL1B

Figure 3. Lung endothelial miR-205-5p controls gene programs implicated in endothelial dysfunction and lung fibrosis, mimicking aberrations of IPF lung ECs. A) Schematics depicting the experimental workflow. Healthy human lung ECs were transfected with negative-control mimic or miR-205-5p mimic and profiled by RNA-seq (created with a licensed version of BioRender.com). **B)** Principal component analysis (PCA) illustrating separation of experimental groups based on the differences in their transcriptomes. **C)** Volcano plot of $-\log_{10}$(FDR *q*) versus $\log_2$(fold change) of genes with respect to miR-205-5p *vs* mimic control; genes that are significantly (FDR *q* <0.05) upregulated (> 2-fold) or downregulated (< 2-fold)in miR-205-5p-overexpressing lung ECs are indicated and tallied in purple and turquoise, respectively.. **D)** Ingenuity Pathway Analysis identifies differentially regulated canonical pathways; pink asterisks indicate pathways whose role in pulmonary fibrosis is known. **E–G)** Heatmaps of differentially regulated genes, including genes responsible for cell cycle regulation (E), endothelial identity and function (F) and proinflammatory and profibrotic genes (G). Colors were assigned after *z*-score-normalizing expression values to a mean of zero and standard deviation of one within each row, with turquoise, white and purple indicating *z*-scores ≤ -2, 0 and ≥ +2, respectively. **H)** Bar plots showing fold-change differences between IPF- *vs* Healthy lung ECs for relevant genes involved in endothelial function and pro-inflammatory/fibrotic state. N=3 independent biological replicates. Data are expressed as mean and SD and p values were calculated using Student's t-test. *p<0.05; **p<0.01; ***p<0.001.

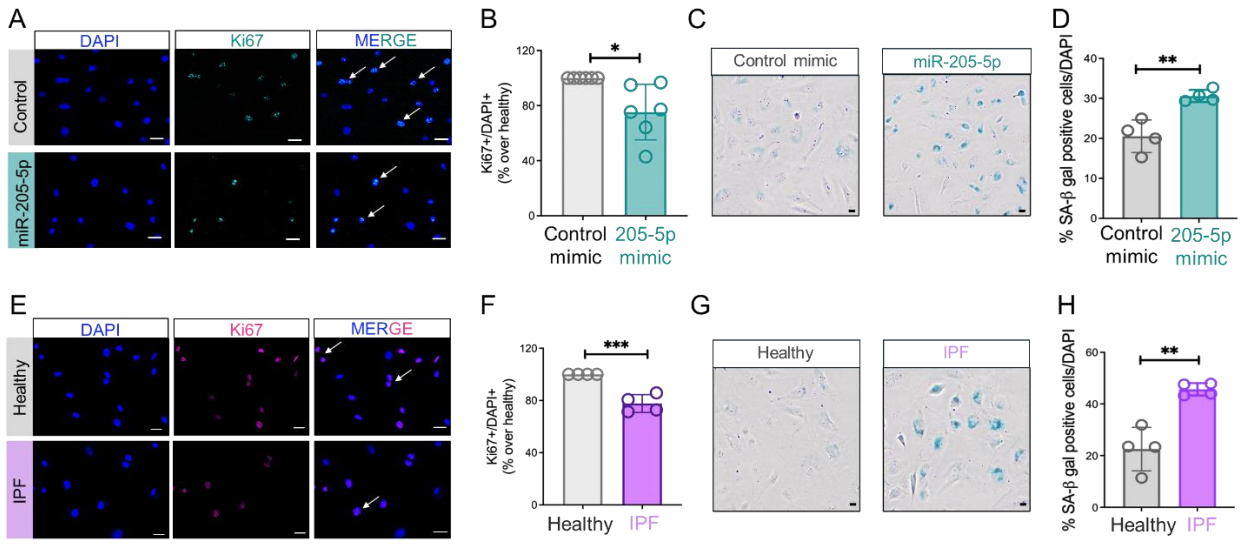

Figure 4. miR-205-5p induces senescence in lung ECs, mirroring cultured IPF lung ECs. A) Representative immunofluorescence images for Ki67 and DAPI in human lung ECs transfected with a miRNA mimic negative control or miR-205-5p mimic. Arrows indicate Ki67+ nuclei. Scale bar: 20 μm. **B)** Quantification of Ki67+ nuclei (normalized to DAPI) reveals a significant reduction in miR-205-5p mimic transfected cells versus control cells. Data are shown as mean ± SD of n = 6 independent biological replicates (average of 3-5 images per replicate) and expressed as percentage over control. p values were calculated using Student's t-test. **C)** Representative SA-β-gal staining images showing positive staining of miR-205-5p overexpressing cells. **D)** Quantification of SA-β-gal positive cells (over total DAPI positive cells) showing increase of SA-β-gal positive cells in miR-205-5p overexpressing lung ECs. Data are shown as mean ± SD of n = 4 independent biological replicates (average of 3-5 images per replicate) and p values were calculated using Student's t-test. **E)** Representative immunofluorescence images for Ki67 and DAPI in healthy- and IPF lung ECs. Arrows indicate Ki67+ nuclei. Scale bar: 20 μm **F)** Quantification of Ki67+ cells normalized to DAPI shows IPF ECs manifesting significant reduced Ki67 staining compared to Healthy lung ECs. Data are shown as mean ± SD of n = 4 independent biological replicates (average of 3-5 images per replicate) and expressed as percentage over

control. p values were calculated using Student's t-test. **G)** Representative SA-β-gal staining images showing positive staining in IPF lung ECs. **H)** Quantification of SA-β-gal positive cells (over total DAPI positive cells) showing increase of SA-β-gal positive cells in IPF lung ECs. Data are shown as mean ± SD of n = 4 independent biological replicates (average of 3-5 images per replicate) and p values were calculated using Student's t-test. *p< 0.05; **p< 0.001.

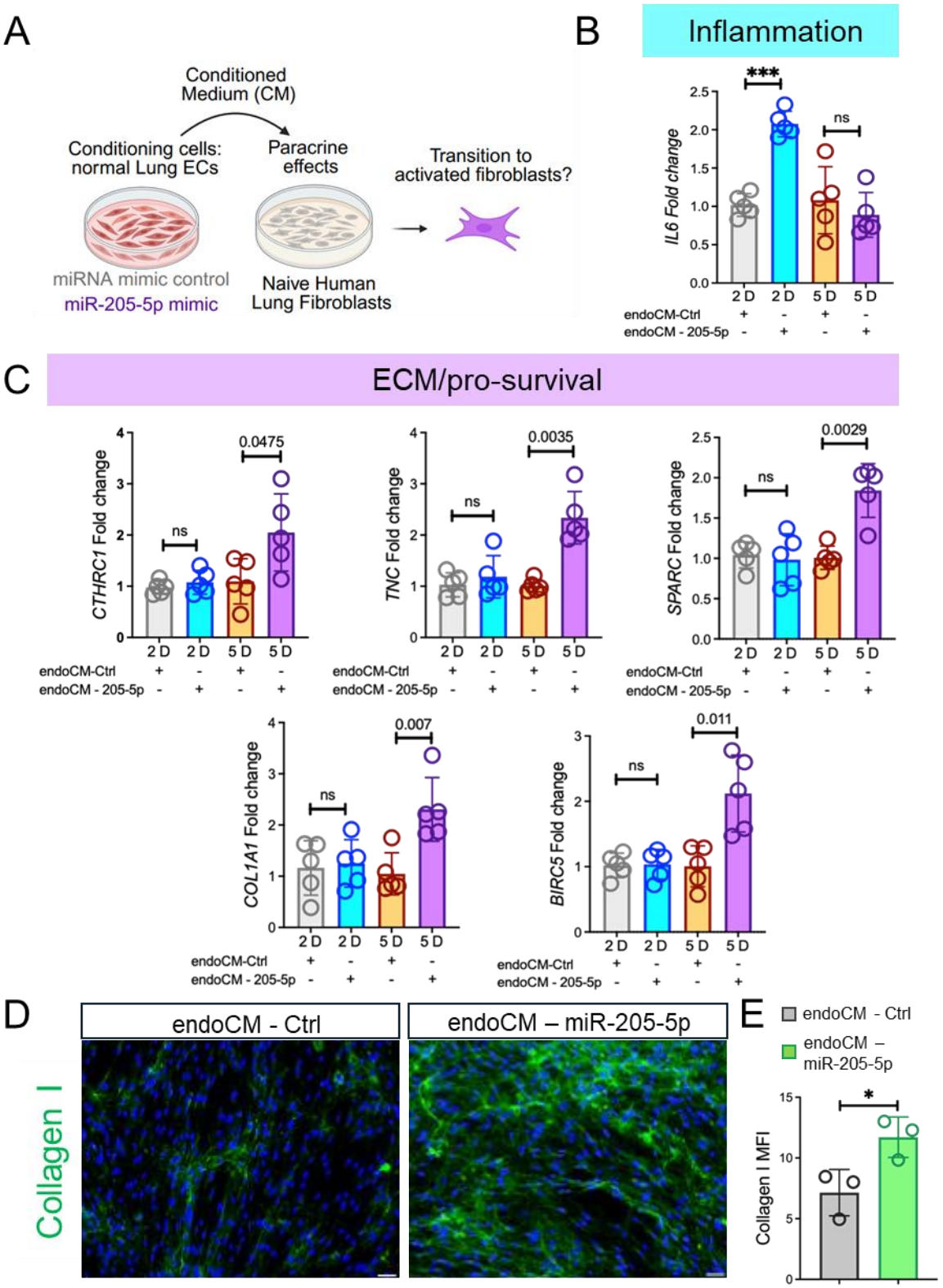
A
Conditioned Medium (CM)
Conditioning cells: normal Lung ECs
Paracrine effects
Transition to activated fibroblasts?
miRNA mimic control
miR-205-5p mimic
Naive Human Lung Fibroblasts
B
Inflammation
IL6 Fold change
***
ns
2 D 2 D 5 D 5 D
endoCM-Ctrl + - + -
endoCM - 205-5p - + - +
C
ECM/pro-survival
CTHRC1 Fold change
0.0475
ns
TNC Fold change
0.0035
ns
SPARC Fold change
0.0029
ns
COL1A1 Fold change
0.007
ns
BIRC5 Fold change
0.011
ns
D
endoCM - Ctrl
endoCM – miR-205-5p
Collagen I
E
endoCM - Ctrl
endoCM – miR-205-5p
Collagen I MFI
*

Figure 5. Lung endothelial miR-205-5p regulates paracrine lung fibroblast activation. A) Healthy lung ECs were transfected with a miRNA mimic negative control or a miR-205-5p mimic. Six hours after transfection, medium was changed to remove transfection reagents. After 3 days, conditioned medium (CM) was collected and applied to recipient healthy human lung fibroblasts for 2 or 5 days (created with a licensed version of BioRender.com). **B-C)** qPCR shows increased expression of pro-inflammatory *IL6* marker at day 2 and ECM/scar-forming fibroblasts genes at day 5 in healthy human lung fibroblasts exposed to CM from miR-205-5p overexpressing lung ECs compared to fibroblasts exposed to CM from lung ECs transfected with miRNA mimic negative control. N=5 independent biological replicates. Data are expressed as mean and SD and p values were calculated using one-way analysis of variance (followed by Tukey's post hoc test). **D)** Representative image of immunostaining for type I collagen in human lung fibroblasts that received CM from control or miR-205-5p overexpressing lung ECs. **E)** Quantification of collagen I staining in D shows increased collagen deposition in recipient human lung fibroblasts exposed to CM from miR-205-5p overexpressing lung ECs. N=3 independent biological replicates, each performed in triplicates. Data are expressed as mean and SD and p values were calculated using Student's t-test. * $p<0.05$; ** $p<0.01$, ***$p<0.001$.

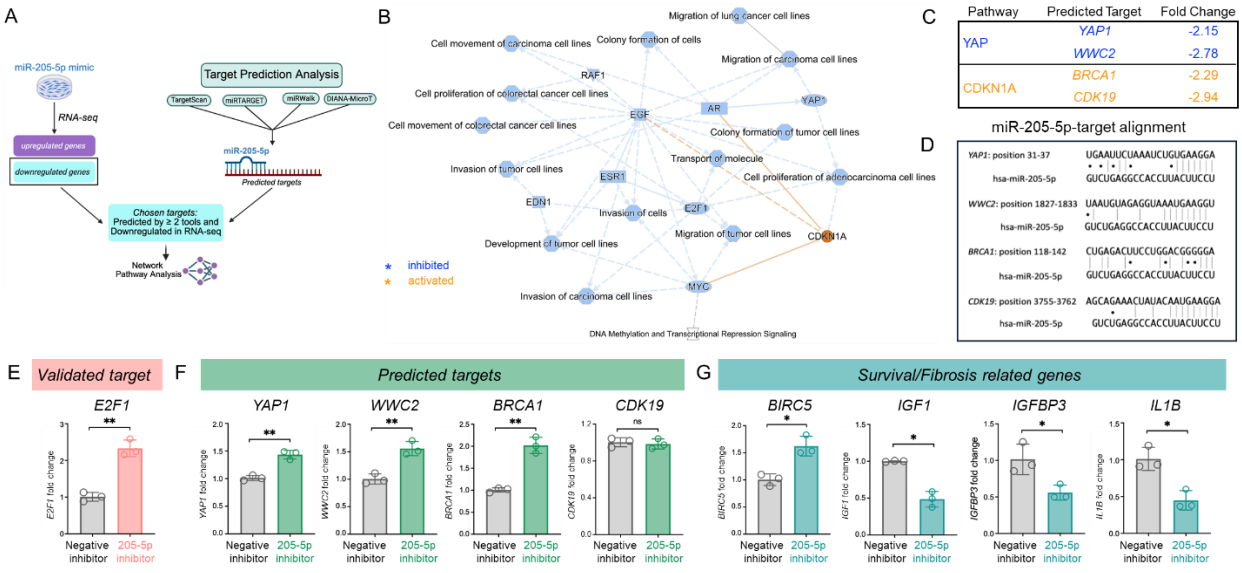

Figure 6. miR-205-5p affects endothelial function potentially by targeting the YAP and CDKN1A cascades, and its inhibition in IPF-lung ECs partially mitigates their pro-fibrotic phenotype. A) Schematic depicting our target prediction analysis workflow (created with a licensed version of BioRender.com). **B)** Network pathway analysis (IPA) of genes predicted to be targets of miR-205-5p in our study. **C)** Selected predicted target genes in YAP and CDKN1A cascades. **D)** Predicted miR:target alignment region. Lines = Watson–Crick base pairs; dots = G:U wobble base pairs. **E-G)** qPCR showing changes in miR-205-5p predicted target genes and genes associated to endothelial dysfunction in IPF lung ECs transfected with a miR-205-5p inhibitor. Inhibition of miR-205-5p leads to the upregulation of the predicted target genes *YAP1*, *WWC2* and *BRCA1*, upregulation of the survival gene *BIRC5* and downregulation of pro-fibrotic genes *IGF1* and *IL1B*. The predicted target gene *CDK19* remains unchanged. N=3 independent biological replicates. Data are expressed as mean and SD and p values were calculated using Student's t-test. *p< 0.05; **p< 0.001.

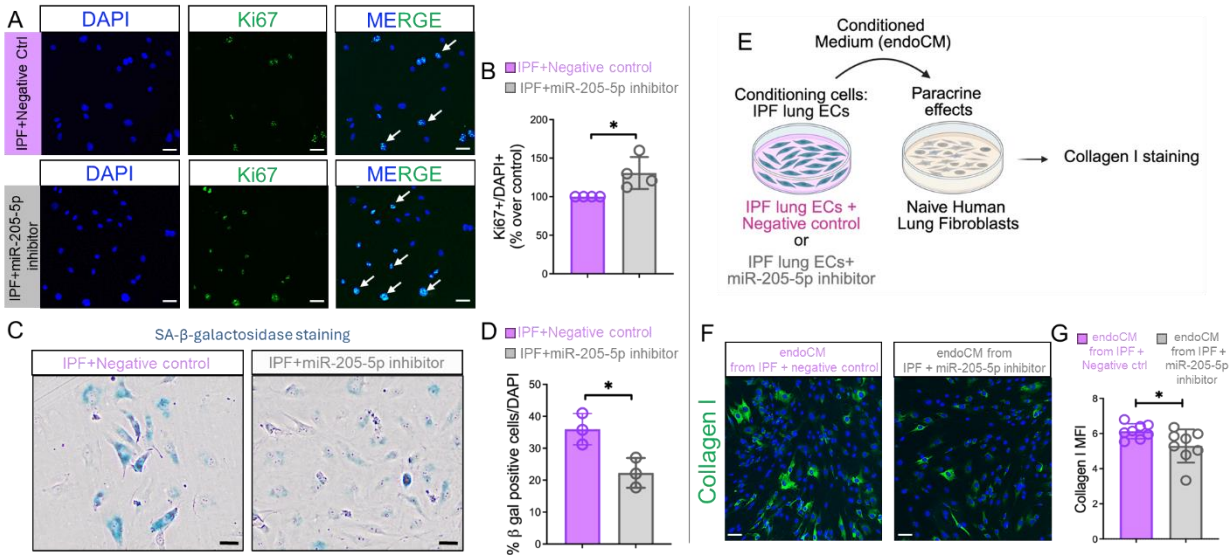

Figure 7. miR-205-5p inhibition attenuates IPF lung ECs senescence and limits paracrine fibroblast activation. A) Representative immunofluorescence images for Ki67 and DAPI in IPF lung ECs transfected with a negative miRNA inhibitor or miR-205-5p inhibitor. Arrows indicate Ki67+ nuclei. Scale bar: 20 μm. **B)** Quantification of Ki67+ nuclei (normalized to DAPI) reveals a significant increase in miR-205-5p inhibited IPF lung ECs versus control transfected IPF cells. Data are shown as mean ± SD of n = 4 independent biological replicates (average of 3-5 images per replicate) and expressed as percentage over control. p values were calculated using Student's t-test. **C)** Representative SA-β-gal staining images showing attenuated staining in miR-205-5p inhibited IPF lung ECs. Scale bar: 20 μm **D)** Quantification of SA-β-gal positive cells (over total DAPI positive cells) showing reduction of SA-β-gal positive cells in miR-205-5p inhibited IPF lung ECs. Data are shown as mean ± SD of n = 3 independent biological replicates (average of 3-5 images per replicate) and p values were calculated using Student's t-test. **E)** IPF lung ECs were transfected with a miRNA inhibitor negative control or a miR-205-5p inhibitor. Six hours after transfection, medium was changed to remove transfection reagents. After 3 days, conditioned medium (CM) was collected and applied to recipient quiescent human lung fibroblasts for 5 days (schematics created with a licensed version of BioRender.com). **F)** Representative images of

immunostaining for type I collagen in human lung fibroblasts that received CM from control IPF lung ECs or upon miR-205-5p inhibition. **G)** Quantification of collagen I staining in E shows decreased collagen deposition in recipient human lung fibroblasts exposed to CM from IPF lung ECs upon inhibition of miR-205-5p. N=8 independent biological replicates, each performed in triplicates. Scale bar: 20 μm Data are expressed as mean and SD and *p* values were calculated using Student's t-test. * $p<0.05$; ** $p<0.01$, *** $p<0.001$.

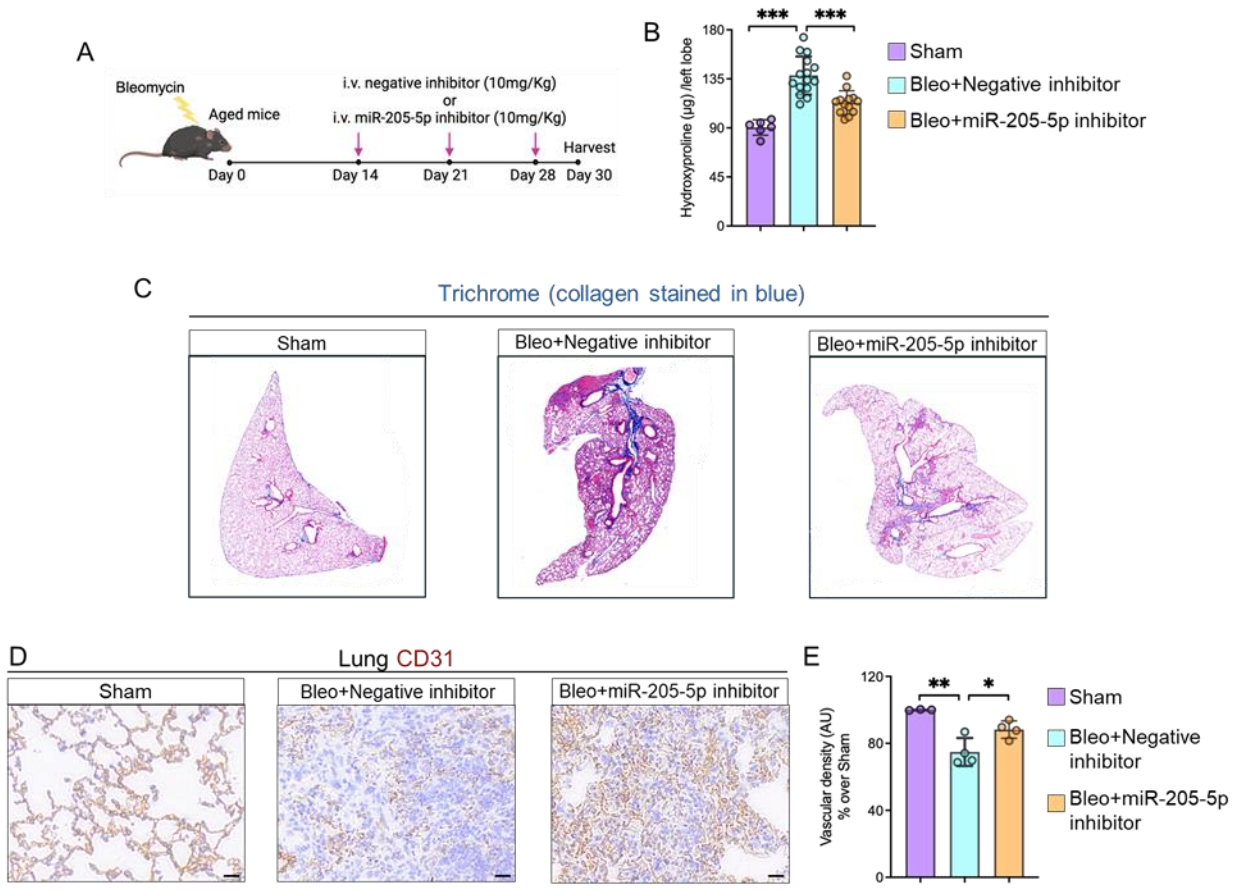

Figure 8. Inhibition of miR-205-5p mitigates fibrosis progression in aged mice challenged with bleomycin.

A) Schematic illustration of the experimental design for the miR-205-5p inhibitor administration, starting at day 14 post-bleomycin injury to assess effects on progression of fibrosis (created with a licensed version of BioRender.com). **B)** Hydroxyproline assay quantifying total collagen content in lungs from sham, bleomycin + negative inhibitor control and bleomycin + miR-205-5p inhibitor at day 30 post-injury. Values are summarized as mean ± SD, *P* values were generated using one-way ANOVA with Tukey's post hoc test for comparison. Sham (n = 11), Bleomycin + negative inhibitor control (n = 12), and Bleomycin + miR-205-5p inhibitor (n = 13). **C)** Representative Masson's Trichrome staining in lung sections from sham, bleomycin-injured control, and bleomycin-injured miR-205-5p inhibitor treated mice at day 30, demonstrating attenuated collagen

(stained in blue) deposition with miR-205-5p inhibition. **D, E)** Immunohistochemistry of mouse lung sections and relative quantification revealed reduced vessel density (CD31 positive) in bleomycin-injured lungs. The vascular network of the lungs of mice treated with miR-205-5p inhibitor was improved compared with that of negative inhibitor treated bleomycin-injured mice. Values are summarized as mean ± SD, *P* values were generated using one-way ANOVA with Tukey's post hoc test for comparison. Each dot represents an individual mouse, and an average of 5-10 field of view each. Sham (n = 3), Bleomycin + negative inhibitor control (n = 4), and Bleomycin + miR-205-5p inhibitor (n = 4).

Tables

Table 1. Human primer sequences for qPCR analysis.

Gene	Forward	Reverse
BIRC5	AGGACCACCGCATCTCTACAT	AAGTCTGGCTCGTTCTCAGTG
BRCA1	GGCTATCCTCTCAGAGTGACATTT	GCTTTATCAGGTTATGTTGCATGG
CCL5	CCAGCAGTCGTCTTTGTCAC	CTCTGGGTTGGCACACACTT
CCN3	AACTGCATTGAACAGACCACA	ATTGACGGTTCCTATTGGTGAC
CDK19	GGATTTGTTTGAGTACGAAGGGT	CTACAAGCCGACATGGATATTCC
COL1A1	AAGGGACACAGAGGTTTCAGTGG	CGGTGGTTTCTTGGTCGGT
CSF3	GCTGCTTGAGCCAACTCCATA	GAACGCGGTACGACACCTC
CTHRC1	CAATGGCATTCCGGGTACAC	GTACACTCCGCAATTTTCCCAA
CXCL10	GTGGCATTCAAGGAGTACCTC	TGATGGCCTTCGATTCTGGATT
E2F1	GAGGAGACCGTAGGTGGGAT	ACAACAGCGGTTCTTGCTCC
IGF1	GCTCTTCAGTTCGTGTGTGGA	GCCTCCTTAGATCACAGCTCC
IGF2	GTGGCATCGTTGAGGAGTG	CACGTCCCTCTCGGACTTG
IGFBP3	AGAGCACAGATACCCAGAACT	GGTGATTCAGTGTGTCTTCCATT
IL1A	TGGTAGTAGCCACCAACGGGA	ACTTTGATTGAGGGCGTCATTC
IL1B	AGCTACGAATCTCCGACCAC	CGTTATCCCATGTGTCGAAGAA
NOS3	TGATGGCGAAGCGAGTGAAG	ACTCATCCATACACAGGACCC
PDGFA	GCAAGACCAGGACGGTCATTT	GGCACTTGACACTGCTCGT
PLVAP	GCTGCTGGTATTACCTGCG	GCCATAGACCATGAAGAGCAC
RPLP0	AGCCCAGAACACTGGTCTC	ACTCAGGATTTCAATGGTGCC
SPARC	CCCATTGGCGAGTTTGAGAAG	CAAGGCCCGATGTAGTCCA
TGFB2	CAGCACACTCGATATGGACCA	CCTCGGGCTCAGGATAGTCT
TNC	AAGAATTGCTCGGAGCCCTAC	TGGGCAGATTTCACGGCTG
WWC2	GTCATTTGCTGATTGTGTTGGG	TGGATCTCTATCTGCGTGGTT
YAP1	CAATAGCTCAGATCCTTTCCT	TAGTATCACCTGTATCCATCTC

Supplemental material legends

Supplemental Figure 1. Lung endothelial miR-205-5p is upregulated in young mice with progressive fibrosis induced by repetitive bleomycin injury. A) Schematics depicting the experimental plan for repetitive bleomycin (created with a licensed version of BioRender.com). Lungs were harvested 90 days after the 6^{th} dose or after the single dose (to allow for complete resolution in single dosed mice). **B)** Lung weight is higher in 6X bleo mice compared to 1X bleo mice. **C)** Representative Masson's Trichrome staining showing increased collagen I deposition (stained in blue) in 6X bleo mice compared to 1X bleo mice. Scale bar: 100μm. **D)** qPCR shows significant upregulation of miR-205-5p in isolated lung ECs from 6X bleo mice compared to lung ECs from 1X bleo mice. snU6 was used as normalization control. Data are expressed as mean and SD and each dot represents an individual mouse (Sham: n=5; 1X Bleo: n=7; 6X Bleo: n=12). p values were calculated using one-way analysis of variance (followed by Tukey's post hoc test). ***p<0.01.

Supplemental Figure 2. miR-205-5p expression is increased in IPF tissue. Quantification of miR-205-5p in healthy and IPF tissue. Individual punctate signals (dots) were quantified using TrackMate in FIJI and counts were normalized to the area of the region of interest. Background signal was subtracted by measuring unstained areas and thresholds were set to minimize noise. Each dot is the average of 12-15 field of views. Values are summarized as mean and SD and *p* values were calculated using Student's t-test.

Supplemental Figure 3. Expression of *CDKN1A* in lung ECs. Violin plot of the expression of senescence marker *CDKN1A* in healthy and IPF CD31+ lung ECs (healthy, n= 1794 cells and IPF n=2830 cells. Values are summarized as mean and SD.

Supplemental Figure 4. Expression of genes not significantly regulated by miR-205-5p in IPF lung ECs. qPCR shows that transcript levels of *TGFB2*, *PDGFA* and *NOS3* are unchanged

in IPF lung ECs upon inhibition of miR-205-5p. N=3 independent biological replicates. Data are expressed as mean and SD and p values were calculated using Student's t-test.

Supplemental Figure 5. Colocalization of miR-205-5p in the mouse pulmonary vasculature. A FAM-labelled miR-205-5p inhibitor (10 mg/Kg) was administered to mice via retro-orbital intravenous injection and lungs were harvested 2 days after the injection. Representative immunofluorescence images show FAM-labelled miR-205-5p inhibitor (green dots) and anti CD31 to identify the vasculature (red). Confocal microscopy reveals colocalization of FAM-labelled miR-205-5p inhibitor within the pulmonary vasculature. Scale bar: 50 μm.

Supplemental Table 1. **List of all predicted target genes from target prediction analysis.**